Title	Effect of R2-FAC development on the ionospheric electric field pattern deduced by a global ionospheric potential solver
Author(s)	Nakamizo, Aoi; Hiraki, Yasutaka; Ebihara, Yusuke; Kikuchi, Takashi; Seki, Kanako; Hori, Tomoaki; Ieda, Akimasa; Miyoshi, Yoshizumi; Tsuji, Yuji; Nishimura, Yukitoshi; Shinbori, Atsuki
Citation	Journal of Geophysical Research: Space Physics (2012), 117(A9)
Issue Date	2012-09
URL	http://hdl.handle.net/2433/193712
Right	©2012. American Geophysical Union.
Type	Journal Article
Textversion	publisher

Effect of R2-FAC development on the ionospheric electric field pattern deduced by a global ionospheric potential solver

Aoi Nakamizo,[1] Yasutaka Hiraki,[2] Yusuke Ebihara,[3] Takashi Kikuchi,[1] Kanako Seki,[1] Tomoaki Hori,[1] Akimasa Ieda,[1] Yoshizumi Miyoshi,[1] Yuji Tsuji,[1] Yukitoshi Nishimura,[4] and Atsuki Shinbori[3]

Received 28 February 2012; revised 20 August 2012; accepted 20 August 2012; published 29 September 2012.

[1] Toward the understanding of the effect of the magnetosphere originated disturbances on the global ionospheric electric field and current system, we developed a two-dimensional ionospheric potential solver based on the so-called "thin shell model." The important extension from the previous studies is that our model covers the pole-to-pole ionosphere without placing any boundary at the equator. By using this solver, we investigate how the ionospheric electric field changes from undershielding condition to overshielding condition as the field aligned current (FAC) distribution changes. Calculations are performed by changing I_{R2}/I_{R1} (the ratio of current intensities of region 2 (R2) and region 1 (R1) FACs) and by moving R2-FAC relative to the fixed R1-FAC. The results are summarized as follows: (1) The turning point, at which the ionosphere turns from undershielding to overshielding is $I_{R2}/I_{R1} = 0.7 \sim 0.8$. (2) With increasing the local time deference between the R1 and R2-FAC peaks, the efficiency of the shielding by R2-FAC increases but the associated potential skews to the nightside. (3) At the same time the shielding effect is weakened around noon, where the R1-potential intrudes to the low latitude region instead, but the R2-potential remains dominant at other local times. The result suggests that the overshielding or undershielding should be identified by observations not only in a limited local time sector but also in the overall ionosphere as much as possible. In order to accurately describe the ionospheric condition, we suggest new classification terms, "complete-overshielding" and "incomplete-overshielding."

Citation: Nakamizo, A., et al. (2012), Effect of R2-FAC development on the ionospheric electric field pattern deduced by a global ionospheric potential solver, *J. Geophys. Res.*, *117*, A09231, doi:10.1029/2012JA017669.

1. Introduction

[2] The momentum and energy transfer between the magnetosphere and ionosphere is primarily achieved by the field-aligned current (FAC) [*Birkeland*, 1908; *Iijima*, 2000]. There are two major large-scale FAC systems at the high latitude region: the region-1 FAC (abbreviated as R1-FAC below) and the region-2 FAC (abbreviated as R2-FAC below) on the equatorward side of R1-FAC [*Iijima and Potemra*, 1976]. Whereas the generation of the FAC itself is one of the most fundamental issues of the magnetospheric physics [e.g., *Tanaka*, 1995; *Iijima*, 2000; *Siscoe et al.*, 2000], it is regarded that R1-FAC is attributed to the solar wind-magnetosphere interaction and R2-FAC originates from the high plasma pressure region in the inner magnetosphere [e.g., *Vasyliunas*, 1970, 1972; *Jaggi and Wolf*, 1973; *Southwood*, 1977; *Ebihara and Miyoshi*, 2011].

[3] The closure of the R2 current in the magnetosphere is described in the fluid approximation in terms of the plasma pressure gradient [e.g., *Vasyliunas*, 1970, 1972; *Jaggi and Wolf*, 1973; *Southwood*, 1977; *Peymirat and Fontaine*, 1994]. Although the ionospheric distributions of the electric field and current are determined through the closure of FACs with the ionospheric currents for a given distribution of the conductance [e.g., *Wolf*, 1970], R1-FAC transmits the large-scale dawn-to-dusk convection electric field driven by the solar wind-magnetosphere, flowing into and away from the ionosphere in the morning and evening sectors, and R2-FAC transmits the dusk-to-dawn electric field in the inner magnetosphere, flowing in the opposite polarity with that of R1-FAC. Because of its opposite sense to the electric field associated with the convection or R1-FAC system, the electric field associated with the inner magnetosphere or R2-FAC system is called the shielding electric field [*Vasyliunas*, 1972; *Jaggi and Wolf*, 1973; *Southwood*, 1977; *Senior and Blanc*, 1984].

[1]Solar-Terrestrial Environment Laboratory, Nagoya University, Nagoya, Japan.
[2]National Institute for Fusion Science, Toki, Japan.
[3]Research Institute for Sustainable Humanosphere, Kyoto University, Uji, Japan.
[4]Department of Atmospheric and Oceanic Sciences, University of California, Los Angeles, California, USA.

Corresponding author: A. Nakamizo, Solar-Terrestrial Environment Laboratory, Nagoya University, Furo-cho, Chikusa-ku, Nagoya 464-8601, Japan. (aoi@stelab.nagoya-u.ac.jp)

0148-0227/12/2012JA017669

[4] The convection electric field can be completely canceled out by the shielding electric field close to the Earth [e.g., *Goldstein*, 2006; *Wolf et al.*, 2007]. In the ionosphere, correspondingly, the electric field associated with R1-FAC is shielded by that of R2-FAC equatorward of the R1 current, which has the opposite polarity. So, poleward and equatorward of the latitude where the shielding region is mapped to, the electric field and current originating the magnetospheric convection and those driven by neutral wind stand out, respectively.

[5] We sometimes observe the disturbances of the magnetospheric origin also in the middle and low latitude regions, along with the variations produced by the neutral wind dynamo. The causes of these disturbances are generally classified into two categories. One of them is explained by the addition of new current systems. The SC current system generated by the magnetospheric response to rapid change of solar wind dynamic pressure [*Araki*, 1994] and the substorm current system associated with the rapid energy release in the night-side plasma sheet [e.g., *Rostoker et al.*, 1980] are such examples. The other is explained by a temporal imbalance between the convection electric field (R1-FAC) and shielding electric field (R2-FAC). Whereas R1-FAC responds relatively instantaneously to changes of the solar wind controlling the convection electric field, R2-FAC tends to delay because it takes a certain time for convection to re-distribute the plasma in the inner magnetosphere. The DP2 type disturbances associated with the quasiperiodic oscillation of IMF-Bz [*Nishida et al.*, 1966; *Nishida*, 1968] and the overshielding associated with the northward change of IMF-Bz [e.g., *Rastogi*, 1977; *Kelley et al.*, 1979] are examples for this type of disturbances.

[6] Following the pioneering works [*Nishida et al.*, 1966; *Rastogi*, 1977], the observational knowledge about the global ionospheric disturbances of the magnetospheric origin have been accumulated [e.g., *Kelley et al.*, 1979; *Araki*, 1994; *Kikuchi et al.*, 1996]. However, we have little modeling studies supplementing these observational findings about the global ionosphere. Thus studies with models treating the ionosphere as a pole-to-pole system in the context of the Magnetosphere-Ionosphere (M-I) coupling are needed. Numerical researches in this context have been considerably made for the high latitude region [e.g., *Kamide and Matsushita*, 1979a, 1979b] and for the sub-auroral region [e.g., *Toffoletto et al.*, 2003]. However, the lower latitude region and how the high latitude and equatorial regions are connected have not been fully investigated numerically. In order to provide the knowledge for the global ionospheric dynamics of the magnetospheric origin, we have developed a global ionospheric potential solver, which we call the GEMSIS-POT solver (Geospace Environment Modeling System for Integrated Studies – POTential solver).

[7] Our model is a two-dimensional potential solver and is basically the same as a so-called "thin shell model," the concept of which has been used in many studies for more than half a century to derive the ionospheric electric field and current distributions [e.g., *Fejer*, 1953; *Tarpley*, 1970, *Maeda and Maekawa*, 1973; *Forbes and Lindzen*, 1976a, 1976b; *Nisbet et al.*, 1978; *Nopper and Carovillano*, 1978; *Harel et al.*, 1981a, 1981b; *Kamide et al.*, 1981; *Senior and Blanc*, 1984; *Tsunomura and Araki*, 1984; *Ahn et al.*, 1986; *Spiro et al.*, 1988; *Tsunomura*, 1999]. The formulation is exactly the same form as described by *Amm* [1996]. This type of the solver has been also used in global MHD codes [e.g., *Tanaka*, 1995; *Janhunen*, 1998; *Gombosi et al.*, 2000]. In those previous studies, the "thin shell model" has been applied only to the high latitude region. *Tsunomura and Araki* [1984] and *Tsunomura* [1999] made the first attempt to apply the solver to the equatorial region, but they solved only one hemisphere with the boundary at the equator. The important extension of our solver from the previous similar studies is that it is applied to the global ionosphere, not only to a polar region, without placing any boundary at the equator.

[8] The overshielding is one of the representative phenomena in which the disturbance of magnetospheric origin prevails in the ionosphere globally. The research is motivated by the observation of the westward turning of the dayside low-latitude electric field, which is usually directed eastward, when the IMF turns northward [*Rastogi*, 1977]. Combining the observational studies [e.g., *Kelley et al.*, 1979; *Kikuchi et al.*, 2000] and modeling studies [e.g., *Senior and Blanc*, 1984; *Peymirat et al.*, 2000], it is now understood that the shielding electric field relevant to R2-FAC overwhelms the convection electric field relevant to R1-FAC when the IMF turns northward after a prolonged interval of southward IMF, as the name implies.

[9] We have many reports on overshielding detection, including the radar measurements in the low latitude region [*Fejer et al.*, 1979, 2007; *Gonzales et al.*, 1979; *Kelley et al.*, 1979; *Spiro et al.*, 1988], simultaneous observation of radar and geomagnetic field measurements [*Kikuchi et al.*, 2000, 2003], SuperDARN observation in the sub-auroral region [*Ebihara et al.*, 2008], and observations during substorms [*Hashimoto et al.*, 2011]. In addition, its magnitude and duration have been investigated in connection with the magnetospheric condition and ionospheric conductance by numerical models [*Jaggi and Wolf*, 1973; *Senior and Blanc*, 1984; *Peymirat et al.*, 2000]. However, it still remains to be addressed quantitatively under what conditions the overshielding occurs and how the corresponding ionospheric electric field distributed theoretically.

[10] In this paper we investigate the overshielding from these perspectives, and also as the first report of GEMSIS-POT. Here the focus is placed on the relative intensity and locations of R1 and R2-FAC. Section 2 describes the details of the solver, section 3 describes the calculation setting and their results, section 4 gives the discussion, and summary is finally given in section 5.

2. Model

2.1. Basic Equation

[11] The concept of the thin shell model is that the ionospheric electric field is determined by imposed source currents (field-aligned currents) under a given conductivity distribution. Although the model does not address the dynamic coupling between the magnetosphere and the ionosphere, it is a useful tool to investigate the ionospheric structure as far as we recognize this point. In section 4, we discuss in detail the limitation and applicability of the model.

[12] As the term "thin shell" indicates, the model is based on the idea that the ionosphere can be regarded as a thin conducting shell with its vertical scale negligible compared with its horizontal scales. The details of its formulation are as

following. We start with the Ohm's law for the weakly ionized gas,

$$\mathbf{j} = \sigma_0 \mathbf{E}_{\parallel} + \sigma_P \mathbf{E}_{\perp} + \sigma_H \hat{\mathbf{b}} \times \mathbf{E}_{\perp}, \tag{1}$$

where $\mathbf{j}$ is the current density, $\mathbf{b}$ is the unit vector along the magnetic field, $\mathbf{E}_{\parallel}$ and $\mathbf{E}_{\perp}$ is the electric fields parallel and perpendicular to the local magnetic field, σ_0 is the parallel, σ_P is the Pedersen, and σ_H is the Hall conductivity.

[13] We adopt the polar coordinate system (θ, φ, z), where θ is the latitude directing northward, φ is the longitude directing eastward, and z is the altitude directing vertically downward. The equation (1) at each point in the ionosphere is rewritten in this coordinate system as

$$\begin{pmatrix} j'_\theta \\ j'_\phi \\ j'_z \end{pmatrix} = \begin{pmatrix} \sigma'_{\theta\theta} & \sigma'_{\theta\phi} & \sigma'_{\theta z} \\ \sigma'_{\phi\theta} & \sigma'_{\phi\phi} & \sigma'_{\phi z} \\ \sigma'_{z\theta} & \sigma'_{z\phi} & \sigma'_{zz} \end{pmatrix} \begin{pmatrix} E'_\theta \\ E'_\phi \\ E'_z \end{pmatrix}, \tag{2a}$$

$$\begin{pmatrix} \sigma'_{\theta\theta} & \sigma'_{\theta\phi} & \sigma'_{\theta z} \\ \sigma'_{\phi\theta} & \sigma'_{\phi\phi} & \sigma'_{\phi z} \\ \sigma'_{z\theta} & \sigma'_{z\phi} & \sigma'_{zz} \end{pmatrix} = \begin{pmatrix} \sigma_P \sin^2 I + \sigma_0 \cos^2 I & -\sigma_H \sin I & (\sigma_0 - \sigma_P) \sin I \cos I \\ \sigma_H \sin I & \sigma_P & -\sigma_H \cos I \\ (\sigma_0 - \sigma_P) \sin I \cos I & \sigma_H \cos I & \sigma_P \cos^2 I + \sigma_0 \sin^2 I \end{pmatrix}, \tag{2b}$$

where I is the dip angle of the local magnetic field. We denote the quantities in the three-dimensional system by the prime in order to avoid the confusion with those in the two-dimensional system described below.

[14] An important assumption for the thin shell model is that the net ionospheric current in the vertical direction is negligibly small ($j'_z \approx 0$), which is consistent with the assumption that the thickness of the ionosphere is much smaller than its horizontal scales. Here we can derive the two-dimensional system from the three-dimensional system in the following way.

[15] By assuming $j'_z = 0$, E'_z can be related to E'_θ and E'_φ as

$$E'_z = \left(-\frac{\sigma'_{z\theta}}{\sigma'_{zz}}\right) E'_\theta + \left(-\frac{\sigma'_{z\phi}}{\sigma'_{zz}}\right) E'_\phi. \tag{3}$$

By using equation (3), the horizontal current in equation (2a) can be related only with the horizontal electric field,

$$\begin{aligned} j'_\theta &= \sigma'_{\theta\theta} E'_\theta + \sigma'_{\theta\phi} E_\phi{}' + \sigma'_{\theta z}\left[\left(-\frac{\sigma'_{z\theta}}{\sigma'_{zz}}\right) E'_\theta + \left(-\frac{\sigma'_{z\phi}}{\sigma'_{zz}}\right) E'_\phi\right] \\ &= \left[\sigma'_{\theta\theta} + \sigma'_{\theta z}\left(-\frac{\sigma'_{z\theta}}{\sigma'_{zz}}\right)\right] E'_\theta + \left[\sigma'_{\theta\phi} + \sigma'_{\theta z}\left(-\frac{\sigma'_{z\phi}}{\sigma'_{zz}}\right)\right] E'_\phi, \end{aligned} \tag{4a}$$

$$\begin{aligned} j'_\phi &= \sigma'_{\phi\theta} E'_\theta + \sigma'_{\phi\phi} E'_\phi + \sigma'_{\phi z}\left[\left(-\frac{\sigma'_{z\theta}}{\sigma'_{zz}}\right) E'_\theta + \left(-\frac{\sigma'_{z\phi}}{\sigma'_{zz}}\right) E'_\phi\right] \\ &= \left[\sigma'_{\phi\theta} + \sigma'_{\phi z}\left(-\frac{\sigma'_{z\theta}}{\sigma'_{zz}}\right)\right] E'_\theta + \left[\sigma'_{\phi\phi} + \sigma'_{\phi z}\left(-\frac{\sigma'_{z\phi}}{\sigma'_{zz}}\right)\right] E'_\phi, \end{aligned} \tag{4b}$$

Then we can rewrite equation (2a) in the following two-dimensional form,

$$\begin{pmatrix} j_\theta \\ j_\varphi \end{pmatrix} = \begin{pmatrix} \sigma_{\theta\theta} & \sigma_{\theta\varphi} \\ \sigma_{\varphi\theta} & \sigma_{\varphi\varphi} \end{pmatrix} \begin{pmatrix} E_\theta \\ E_\varphi \end{pmatrix}, \tag{5a}$$

$$\sigma_{\theta\theta} = \sigma'_{\theta\theta} + \sigma'_{\theta z}\left(-\frac{\sigma'_{\theta z}}{\sigma'_{zz}}\right) = \frac{\sigma_P \sigma_0}{\sigma_P \cos^2 I + \sigma_0 \sin^2 I}, \tag{5b}$$

$$\sigma_{\theta\phi} = \sigma'_{\theta\phi} + \sigma'_{\theta z}\left(-\frac{\sigma'_{z\phi}}{\sigma'_{zz}}\right) = -\frac{\sigma_H \sigma_0 \sin I}{\sigma_P \cos^2 I + \sigma_0 \sin^2 I}, \tag{5c}$$

$$\sigma_{\phi\theta} = \sigma'_{\phi\theta} + \sigma'_{\phi z}\left(-\frac{\sigma'_{z\theta}}{\sigma'_{zz}}\right) = \frac{\sigma_H \sigma_0 \sin I}{\sigma_P \cos^2 I + \sigma_0 \sin^2 I} = -\sigma_{\theta\phi}, \tag{5d}$$

$$\sigma_{\phi\phi} = \sigma'_{\phi\phi} + \sigma'_{\phi z}\left(-\frac{\sigma'_{z\phi}}{\sigma'_{zz}}\right) = \sigma_P + \frac{{\sigma_H}^2 \cos^2 I}{\sigma_P \cos^2 I + \sigma_0 \sin^2 I}. \tag{5e}$$

[16] Another important assumption of the thin shell model is that the vertical variations of horizontal electric fields are negligibly small. Under this assumption, we can perform the height-integration of the above equations independent of electric field. Then the final form of the Ohm's law in the two-dimensional ionosphere is

$$\begin{aligned} \begin{pmatrix} J_\theta \\ J_\phi \end{pmatrix} &= \begin{pmatrix} \Sigma_{\theta\theta} & \Sigma_{\theta\phi} \\ \Sigma_{\phi\theta} & \Sigma_{\phi\phi} \end{pmatrix} \begin{pmatrix} E_\theta \\ E_\phi \end{pmatrix}, \quad or \quad \mathbf{J} = \boldsymbol{\Sigma} \bullet \mathbf{E} \\ &= \boldsymbol{\Sigma} \bullet (-\nabla \Phi), \end{aligned} \tag{6a}$$

$$\Sigma_{\theta\theta} = \int \sigma_{\theta\theta} = \int \frac{\sigma_P \sigma_0}{\sigma_P \cos^2 I + \sigma_0 \sin^2 I}, \tag{6b}$$

$$\Sigma_{\theta\phi} = -\Sigma_{\phi\theta} = \int \sigma_{\theta\phi} = -\int \frac{\sigma_H \sigma_0 \sin I}{\sigma_P \cos^2 I + \sigma_0 \sin^2 I}, \tag{6c}$$

$$\Sigma_{\phi\phi} = \int \sigma_{\phi\phi} = \int \left(\sigma_P + \frac{{\sigma_H}^2 \cos^2 I}{\sigma_P \cos^2 I + \sigma_0 \sin^2 I}\right), \tag{6d}$$

where $\mathbf{J}$ is the height-integrated current density, $\boldsymbol{\Sigma}$ is the height-integrated conductivity tensor, $\mathbf{E}$ is the electric field, and Φ is the electric potential, in the two-dimensional ionosphere.

[17] The ionospheric horizontal current $\mathbf{J}$ is related to the FAC, via the current continuity relation, as

$$\nabla \bullet \mathbf{J} = j_{\parallel} \sin I, \tag{7}$$

where, $j_{\parallel}$ is the density of the FAC (positive for downward). From (6a) and (7), we finally obtain

$$-j_{\parallel} \sin I = \nabla \bullet (\boldsymbol{\Sigma} \bullet \nabla \Phi). \tag{8}$$

Thus Φ can be given as the solution of a two-dimensional Poisson equation with $j_{\parallel}$ as a source and the background conductivity distribution $\mathbf{\Sigma}$ as a coefficient.

2.2. Computational Grid and Input Parameters

[18] We adopt a longitude (φ)-latitude (θ) coordinate system. We solve (6) for both hemispheres without placing any boundary at the equator. This is one of the most important extensions of our model from previous studies [e.g., *Tsunomura and Araki*, 1984; *Tsunomura*, 1999]. The spatial resolution can be adjusted depending on the target of the study.

[19] We set the global conductivity distribution in the following way. At first the values of σ_0, σ_P, and σ_H at each point and height are calculated by using the neutral gas temperature and number densities of neutral species obtained from the NRLMSISE-00 model [*Picone et al.*, 2002] and temperatures and number densities of charged particles obtained from the IRI-2007 model [*Bilitza and Reinisch*, 2008]. Here we referred to *Schunk and Walker* [1973] and *Schunk and Nagy* [1978] for collision frequencies and referred to *Brekke and Moen* [1993] for the calculation formulae. As for the ambient magnetic field, the IGRF-2005 reference model or dipole field is used. Next, $\Sigma_{\theta\theta}$, $\Sigma_{\varphi\varphi}$, and $\Sigma_{\theta\varphi}$ are calculated based on (6b), (6c), and (6d). Here the height integration is taken from 90 to 300 km in altitude over the entire ionosphere.

[20] The height-integrated conductivity includes an unrealistic enhancement in the low latitude region arising inevitably from the thin shell approximation. Here we perform the following conductivity modification suggested by *Tsunomura* [1999].

[21] 1. $\Sigma_{\theta\theta}$: The value at the equator is deduced by extrapolating the value at +/−1° in latitude with the gradient over 2° in latitude. As we can see in the expression (5b), $\sigma_{\theta\theta}$ asymptotically approaches to σ_0 as the dip angle I approaches 0° and consequently the height integration of $\sigma_{\theta\theta}$ becomes equal to that of σ_0. As a result, $\Sigma_{\theta\theta}$ becomes artificially quite large at the equator. This is the reason of this modification.

[22] 2. $\Sigma_{\varphi\varphi}$: The values in the equatorial region are increased by a factor of 1.2 at the equator, 1.8 at 1° latitude, and 2 at 2° in latitude. For latitudes higher than 2°, the multiplication factor is linearly decreased with increasing latitude to unity at 25° latitude. This intensification and broadening is based on the consideration that the thin shell model cannot realistically (well) reproduce the eastward current in the equatorial region. It has been known that the eastward current in the equatorial region calculated by models including the meridional current system in the equatorial region driven by an eastward electric field [*Untiedt*, 1967; *Richmond*, 1973] or by a three-dimensional model in the equatorial region [*Forbes and Lindzen*, 1976a, 1976b] is larger and wider than that of the thin shell model [*Sugiura and Cain*, 1966]. The existence of the meridional current system is also evidenced by the observations [*Musmann and Seiler*, 1978; *Maeda et al.*, 1982]. These modeling and observational results suggest that $\Sigma_{\varphi\varphi}$ should be enhanced and broadened in order to disguise the effect of the meridional current system. Based on the comparison between the meridional current system model and the thin shell model for the height-integrated eastward current [*Untiedt*, 1967, Figure 7], *Tsunomura* [1999] introduced the aforementioned multiplication factors.

[23] 3. $\Sigma_{\theta\varphi}$: The modification of $\Sigma_{\theta\varphi}$ is also related to the consideration of the meridional current system in the equatorial region driven by the east–west electric field E'_{φ}. In the expression of $\sigma_{\theta\varphi}$ of equation (5c), the first term is simply the original contribution of external E'_{φ} to j_{θ} but the second term is the contribution through the vertical field E'_z, as we can understand by equations (3) and (4a). This E'_z is an algebraic product arising from the assumption of $j'_z = 0$, and is equivalent to a polarization electric field. The vertical electric field E'_z includes the component parallel to the ambient magnetic field except at the dip equator. In most cases, the parallel component of the electric field is kept close to zero because of the high conductivity in the magnetic field direction. The problem here is that the thin shell approximation inevitably introduces a finite electric field along the field line through the polarization field E'_z and produces an artificial north–south ionospheric current. Therefore, the contribution of E'_z to j_{θ} as described in the second term of equation (5c) (the fourth term of the right side of equation (4a)) should be reduced in order to avoid the unrealistic enhancement of j_{θ}. The reduction factor of the second term of equation (5c) that gives more realistic values of $\Sigma_{\theta\varphi}$ near the equator was determined by trial and error by *Tsunomura* [1999]: The reduction rate is 1.0 just at the neighborhood of the equator and decreases linearly with increasing latitude to zero at 30° latitude. By introducing this factor in the course of the height integration of $\sigma_{\theta\varphi}$, we calculate $\Sigma_{\theta\varphi}$. The above remarks are concerned with the features of the polarization electric field E'_z driven by the external east–west component of the electric field E'_{φ}. The discussion about $\Sigma_{\varphi\theta}$, that is, polarization electric field E'_z driven by the external north-south component of the electric field E'_{θ} is remained. According to *Untiedt* [1967], E'_{θ} does not contribute to the meridional current very significantly. This means the modification used for $\Sigma_{\theta\varphi}$ does not have to be used for $\Sigma_{\varphi\theta}$. However, according to *Tsunomura* [1999], the calculated ionospheric electric field and current do not change very much by using the similar modulation for $\Sigma_{\varphi\theta}$ because the relating component of the electric field (E_{θ}) is very small in the low latitude region.

[24] Although the above modification is based on the thought that we should reduce the effect of the parallel electric field ($\mathbf{E}_{\parallel}$), it is not any general rule that $E_{\parallel}$ should be zero. For example, $\mathbf{E}_{\parallel}$ is inevitably required if we consider the 3-D closure of field-aligned current to the Pedersen and Hall current inside the ionosphere. The recently proposed 3-D model of the Cowling channel [*Yoshikawa*, 2007; *Fujii et al.*, 2011; *Yoshikawa et al.*, 2011a] is an example of such a current system. However, the point here is that, in most cases, the parallel electric field is practically close to zero compared with E_{θ} and E_{φ}, because σ_0 is quite high compared with σ_P and σ_H. Thus we need to reduce the effect of needlessly large $\mathbf{E}_{\parallel}$ produced by the vertical polarization effect.

[25] Finally the conductivity enhancement in auroral region is superposed on the calculated $\mathbf{\Sigma}$. At present we use an empirical model based on the electron precipitation intensity sorted by the Kp index provided by *Hardy et al.* [1987]. Thus the derived Pedersen and Hall conductivity are added to the diagonal part ($\Sigma_{\theta\theta}$ and $\Sigma_{\varphi\varphi}$) and the non-diagonal part ($\Sigma_{\theta\varphi}$, $\Sigma_{\varphi\theta} = -\Sigma_{\theta\varphi}$), respectively.

[26] This model allows setting the distribution of FAC in a flexible way. This is the second important extension from

previous studies [e.g., *Tsunomura and Araki*, 1984; *Tsunomura*, 1999]. (The distribution used in this study is described in the next section 3.1.) Finally, equation (8) is solved by the combination of the Multigrid and Successive Over-Relaxation (SOR) method with input parameters mentioned here.

3. Calculation and Results

[27] In this section we investigate how the ionosphere changes from undershielding condition to overshielding condition as the FAC distribution changes. First we describe the calculation setting (section 3.1) then we show the calculation results. A focus is placed on the dependence of the electric field pattern on the intensity of R2-FAC (section 3.2) and on the intensity and peak local times of R2-FAC (section 3.3).

3.1. Calculation Setting

[28] The spatial resolution of the computational grid is set at 1.4° for the φ-direction and 0.7° for the θ-direction; the number of grid points is 256 × 256. We use the conductivity distribution for an equinox condition with Kp = 5. The dipole field is used as the ambient magnetic field for simplicity.

[29] We distribute R1-FAC following a Gaussian function in a similar way to previous studies [e.g., *Kamide and Matsushita*, 1979a; *Tsunomura*, 1999]. In this study, we also distribute R2-FAC additionally. Their functional forms are

$$j_{||,R1} = \pm j_{0,R1} \exp\left[-\frac{(\theta-\theta_{0,R1})^2}{\delta_{\theta,R1}^2} - \frac{(\phi \mp \phi_{0,R1})^2}{\delta_{\varphi,R1}^2}\right], \quad (9a)$$

$$j_{||,R2} = \pm j_{0,R2} \exp\left[-\frac{(\theta-\theta_{0,R2})^2}{\delta_{\theta,R2}^2} - \frac{(\varphi \pm \varphi_0, R2)^2}{\delta_{\varphi,R2}^2}\right], \quad (9b)$$

where the subscripts "R1" and "R2" denote R1 and R2-FAC, $j_{0,R1}$ and $j_{0,R2}$ are the peak current densities, $\theta_{0,R1}$ and $\theta_{0,R2}$ are the peak latitudes, $\varphi_{0,R1}$ and $\varphi_{0,R2}$ are the peak longitudes, $\delta_{\theta,R1}$ and $\delta_{\theta,R2}$ are the latitudinal e-folding distance, $\delta_{\varphi,R1}$ and $\delta_{\varphi,R2}$ are the longitudinal e-folding distance widths, and the upper and lower signs are taken for the currents flowing into and away from the ionosphere, respectively.

[30] The parameters for R1-FAC, $j_{0,R1}$, $\varphi_{0,R1}$, $\delta\theta_{0,R1}$, and $\delta\varphi_{0,R1}$, are determined based on an empirical distribution [*Hori et al.*, 2009] except that $\theta_{0,R1}$ is chosen in a way described below along with that of R2-FAC. In order to simplify the problem, we fix R1-FAC both in the intensity and spatial distribution, as well as the conductivity distribution, and investigate how the ionospheric electric field changes depending on the intensity and longitudinal distribution of R2-FAC. Finally we slightly adjust the peak latitudes $\theta_{0,R1}$ and $\theta_{0,R2}$ in such a way that both R1 and R2-FACs are confined inside the auroral region, which is represented by conductivity enhancements in Hardy's model [*Hardy et al.*, 1987]. Specifically, for the northern hemisphere, R1-FAC is fixed with $\theta_{0,R1}$ = 70°, $\varphi_{0,R1}$ = 135° (equals to 09:00 and 15:00 in local time), $\delta_{\theta,R1}$ = 2°, and $\delta_{\varphi,R1}$ = 45°. As for R2-FAC, the peak latitude and decay widths are fixed as $\theta_{0,R2}$ = 62°, $\delta_{\theta,R2}$ = 2°, $\delta_{\varphi,R2}$ = 45°. The peak latitude $\varphi_{0,R2}$ is changed from 135° (09:00 and 15:00 in LT, equals to that of R1-FAC) to 90° (06:00 and 18:00 in LT, purely dawn and dusk) with a step difference of 15° (one hour).

[31] The peak current densities $j_{0,R1}$ and $j_{0,R2}$ are determined as follows. When we set both R1 and R2-FACs, the net balance of an upward or downward FACs in a given point is different from the current given by the original Gaussian function because it overlaps with other Gaussian functions. This effect depends on the relative intensities and locations of the distributions. R1 or R2-FACs are partially canceled by their own counterparts on the opposite side of the noon-midnight meridian and also by each other in the same local time sector. In order to make the subject of the calculation clear, we keep the net intensity of R1-FAC constant and change the ratio of net intensities of R2 and R1-FACs from 0.0 (no R2-FAC) to 1.3 (strong R2-FAC) with an increment of 0.1. $j_{0,R1}$ and $j_{0,R2}$ are adjusted as a function of $\varphi_{0,R2}$ (peak longitudes (local times) of R2-FAC) and the ratio of net intensities of R2 and R1-FACs. We distribute R1 and R2-FAC in the southern hemisphere symmetrically with respect to the equator.

[32] Thus adjusted peak current densities $j_{0,R1}$ and $j_{0,R2}$ are summarized in Table 1. I_{R1} and I_{R2} are the absolute values of the net current intensities of R1 and R2-FACs in the northern and morning hemisphere, respectively. The top row is the ratio of I_{R2} to I_{R1}. The subsequent rows list the ratio of $j_{0,R2}$ to $j_{0,R1}$, $j_{0,R1}$, and $j_{0,R2}$ corresponding to each I_{R2}/I_{R1} (the ratio of I_{R2} to I_{R1}) and $\varphi_{0,R2}$ (peak longitudes (local times) of R2-FAC) pair. The area of R2-FAC is larger than that of R1-FAC because R2-FAC is distributed on the equatorward side of R1-FAC with the same functional form and e-folding widths. Therefore $j_{0,R2}/j_{0,R1}$ tends to become small relative to I_{R2}/I_{R1}. The total upward and downward FAC intensities of R1-FAC as well as those of R2-FAC are balanced because we distribute them symmetrically with respect to the noon-midnight meridian as well as to the equator.

[33] Figure 1 shows the polar distributions of input parameters. Each panel adopts the same format with noon being to the left and dawn to the top. The center and outer most circles are the northern pole and the 0° latitude (equator). Circles are added at 60° and 30° in latitude, supplementary. Figures 1a, 1b, and 1c show $\Sigma_{\theta\theta}$, $\Sigma_{\varphi\varphi}$, and $\Sigma_{\theta\varphi}$ in a logarithmic scale. The color scale is identical with each other in these three plots, while the maximum and minimum values are shown at the top-right of each plot. Figure 1d shows FACs distribution. (The downward current is taken to be positive.) The R2-FAC distribution with I_{R2}/I_{R1} of 0.5 and $\varphi_{0,R2}$ of 135° (09:00 and 15:00 in LT, equals to that of R1-FAC) is shown as an example; calculations are performed for all distributions listed in Table 1.

3.2. Dependence on the Intensity of R2-FAC

[34] First we investigate how the intensity of R2-FAC affects the ionospheric electric field. As we mentioned in section 3.1, we fix R1-FAC both in the intensity and spatial distribution, and conductivity distribution. We increase the R2-FAC intensity by changing I_{R2}/I_{R1} from 0.0 to 1.3 with an increment of 0.1 as listed in Table 1. The peak local times of R2-FAC are fixed at 09:00 and 15:00 with $\varphi_{0,R2}$ = 135° in the same way as we did for R1-FAC.

[35] Figure 2 shows the input parameters and obtained electrostatic potential patterns. The cases with I_{R2}/I_{R1} of 0.0, 0.4, 0.7, 0.8, 1.1, and 1.3 are shown in Figures 2a–2a′ to 2f–2f′, respectively, in the same coordinate system as Figure 1. In Figures 2a–2f FACs distributions are shown in

Table 1. The Adjusted Peak Current Densities $j_{0,\,R1}$ and $j_{0,\,R2}$ in Gaussian Functions of FACs

		Ratio of I_{R2} to I_{R1}[a]													
	R1 and R2-FAC[b]	0.0	0.1	0.2	0.3	0.4	0.5	0.6	0.7	0.8	0.9	1.0	1.1	1.2	1.3
$\varphi_{0,\,R2}$[c] = 135°	$j_{0,\,R2}/j_{0,\,R1}$	0.000	0.074	0.147	0.220	0.292	0.365	0.438	0.510	0.583	0.656	0.728	0.801	0.874	0.946
	$j_{0,\,R1}$	1.600	1.601	1.601	1.602	1.603	1.603	1.604	1.605	1.605	1.606	1.607	1.607	1.608	1.608
	$j_{0,\,R2}$	0.000	0.119	0.235	0.352	0.468	0.585	0.702	0.819	0.936	1.053	1.170	1.287	1.405	1.522
$\varphi_{0,\,R2}$ = 120°	$j_{0,\,R2}/j_{0,\,R1}$	0.000	0.066	0.132	0.197	0.262	0.327	0.392	0.457	0.522	0.587	0.652	0.718	0.783	0.848
	$j_{0,\,R1}$	1.600	1.601	1.601	1.602	1.602	1.603	1.604	1.604	1.605	1.605	1.606	1.607	1.607	1.608
	$j_{0,\,R2}$	0.000	0.106	0.211	0.315	0.419	0.524	0.628	0.733	0.838	0.943	1.048	1.153	1.258	1.363
$\varphi_{0,\,R2}$ = 105°	$j_{0,\,R2}/j_{0,\,R1}$	0.000	0.064	0.126	0.189	0.251	0.313	0.376	0.438	0.501	0.563	0.626	0.688	0.751	0.813
	$j_{0,\,R1}$	1.600	1.601	1.601	1.602	1.602	1.603	1.603	1.604	1.604	1.605	1.606	1.606	1.607	1.607
	$j_{0,\,R2}$	0.000	0.102	0.202	0.302	0.402	0.502	0.603	0.703	0.803	0.904	1.004	1.105	1.206	1.306
$\varphi_{0,\,R2}$ = 90°	$j_{0,\,R2}/j_{0,\,R1}$	0.000	0.063	0.125	0.187	0.246	0.310	0.372	0.434	0.496	0.558	0.620	0.681	0.743	0.805
	$j_{0,\,R1}$	1.600	1.600	1.601	1.601	1.602	1.602	1.603	1.603	1.604	1.604	1.605	1.605	1.606	1.606
	$j_{0,\,R2}$	0.000	0.101	0.200	0.299	0.398	0.497	0.597	0.696	0.795	0.895	0.994	1.094	1.193	1.293

[a] I_{R1} and I_{R2} are current intensities of R1 and R2-FAC integrated for Northern and morning hemisphere. I_{R1} is fixed with 1.6621 [10^6 A] (integrated for Northern and morning hemisphere).
[b] Peak current densities of R1 and R2-FAC [μA/m^2]. See equations (9a) and (9b).
[c] Peak longitude of Gaussian function of R2-FAC. See equation (9b).

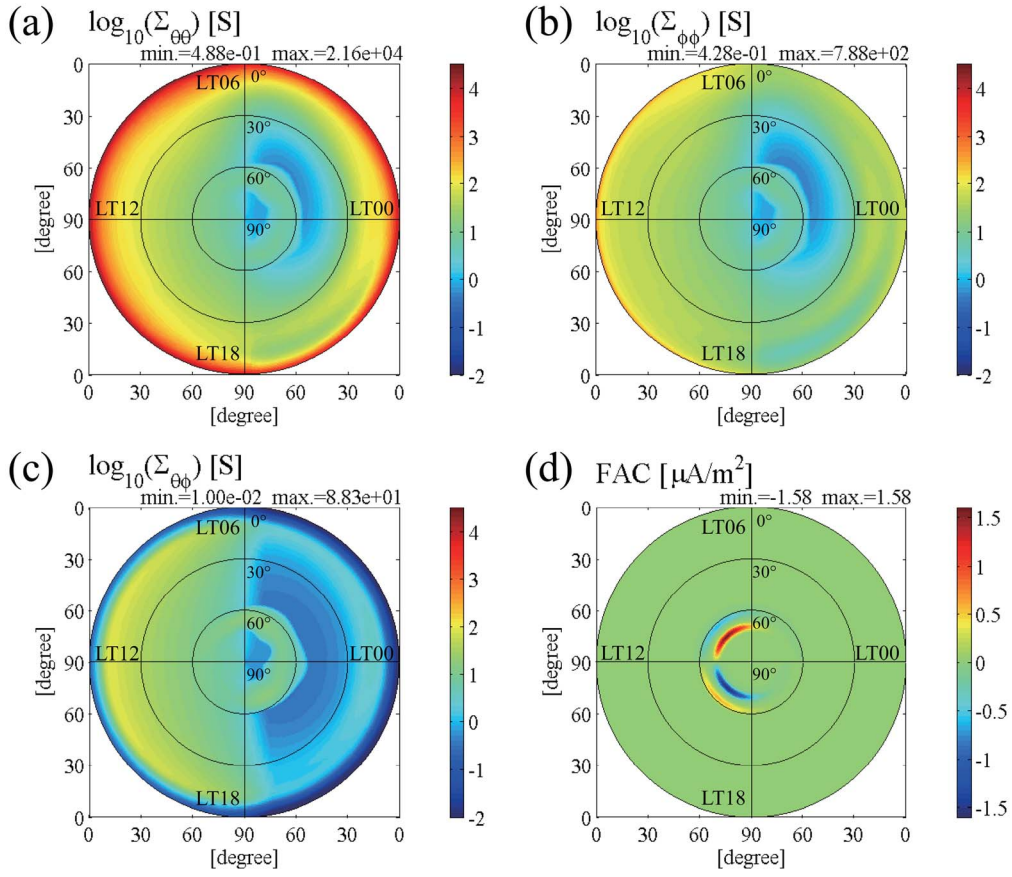

Figure 1. Polar distributions of input parameters. Each panel adopts the same format with noon being to the left and dawn to the top. Center and outer most circles are the northern pole and 0° latitude (equator). Circles are added at 60° and 30° in latitude. (a–c) $\Sigma_{\theta\theta}$, $\Sigma_{\varphi\varphi}$, and $\Sigma_{\theta\varphi}$ shown in a logarithmic scale. The color scale is identical with each other in these three plots. (d) FACs distribution. The downward current is taken to be positive. The R2-FAC distribution with I_{R2}/I_{R1} of 0.5 and $\varphi_{0,R2}$ of 135° (09:00 and 15:00 in LT, equals to that of R1-FAC) is shown as an example. Maximum and minimum values are shown at the top-right of each plot.

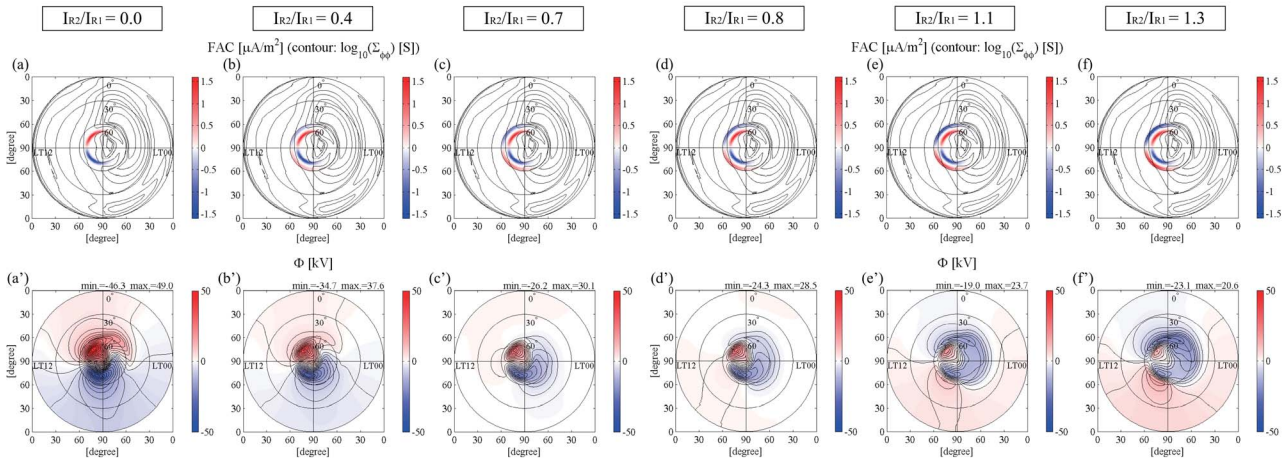

Figure 2. Input parameters and obtained electrostatic potential patterns. The cases with I_{R2}/I_{R1} of 0.0, 0.4, 0.7, 0.8, 1.1, and 1.3 are shown in the same coordinate system (format) as Figure 1. (a–f) FACs distributions shown in color and one component of the conductivity tensor, $\Sigma_{\varphi\varphi}$, shown by contour lines. (a′–f′) The corresponding electric potential patterns. Maximum and minimum values of electric potential are given at the top-right of each panel.

color and one component of the conductivity tensor, $\Sigma_{\varphi\varphi}$, is shown by contour lines as a reference of background conductivity. The corresponding electric potential patterns are shown in Figures 2a′–2f′. The maximum and minimum values of electric potential are given at the top-right of each panel.

[36] Figure 2a′ shows the potential pattern for the most simplified FACs distribution with no R2-FAC. The positive and negative electric potential are formed in the morning and afternoon sides with their peaks around 08:00 LT and 17:00 LT, corresponding to the distributed R1-FAC. The equi-potential lines extend from polar region to the equator with no deformation, indicating that the electric field imposed by R1-FAC purely penetrates from the polar region to equatorial region. The ionosphere is entirely dominated by this R1-sense electric field. The equatorial electric field is directed eastward and westward in the dayside and nightside, respectively.

[37] The ionospheric condition dominated by R1-FAC is gradually deformed as the R2-FAC intensity increases. In Figure 2b′, the result for I_{R2}/I_{R1} = 0.4, the overall electric field still has the same sense but it is weakened relative to Figure 2a′. Electric fields across the polar region (the potential drop in the polar region) and lower latitude region are reduced as compared to those of Figure 2a′, as indicated by the maximum and minimum values and the sparseness of contour lines. That is, the R1-sence electric field is partially shielded by R2-FAC imposed on the equatorward side of R1-FAC. In Figures 2c′ and 2d′, the results with I_{R2}/I_{R1} = 0.7 and 0.8, we can see the effect of R2-FAC more clearly. In addition to the decrease of the potential drop across the polar region, the potential pattern by R2-FAC starts to appear on the equatorward side and in the opposite sense to the pre-existing electric potential by R1-FAC. In Figure 2c′ (I_{R2}/I_{R1} = 0.7), almost all equi-potential lines on the dayside are closed inside the polar region, indicating that the R1-electric field is almost completely shielded by the R2-electric field. In Figure 2d′ (I_{R2}/I_{R1} = 0.8), on the other hand, a few equi-potential lines originating with the R2-potential extend to the low-latitude and equatorial regions, indicating that the ionospheric electric field equatorward side of FACs now has the R2-sense. Thus, under these input parameters, the ionosphere changes from an undershielding condition to an overshielding condition between I_{R2}/I_{R1} = 0.7 and I_{R2}/I_{R1} = 0.8. The effect of R2-FAC becomes more significant in Figures 2e′ (I_{R2}/I_{R1} = 1.1) and 2f′ (I_{R2}/I_{R1} = 1.3). In Figure 2e′ the R2-potential pattern becomes clear and some of the equi-potential lines originated from it extends to the lower latitude and equatorial region. In Figure 2f′, the R2-electric field overwhelms the R1-electric field as indicated by dense contour lines and the deep color around R2-FAC. In these panels, the electric field in the equatorward side of the location of FACs is entirely in opposite sense to that of R1-dominated ionosphere (Figures 2a′ and 2b′). That is, Figure 2e′ provides an example for strong overshielding and Figure 2f′ is an extreme example of overshielding.

[38] Figures 3a and 3b show the local time profiles of the longitudinal electric field component, E_φ, along the equator and the latitudinal profiles along the noon meridian, respectively, which we extracted from two-dimensional patterns shown in Figure 2. E_φ is positive eastward. The black, blue, green, yellow, magenta, and red colors represent the cases with I_{R2}/I_{R1} of 0.0, 0.4, 0.7, 0.8, 1.1, and 1,3, corresponding to Figures 2a′ and 2f′, respectively.

[39] The local time profiles basically show bipolar patterns with their peaks around the noon and midnight, reversing their signs between dayside and nightside. In the most simplified case with I_{R2}/I_{R1} = 0.0, the electric field is eastward in the dayside and westward in the nightside (see also Figure 2a′). The amplitude decreases with increasing I_{R2}/I_{R1} from 0.0 to 0.7, but the local-time profile is qualitatively the same as the case with I_{R2}/I_{R1} = 0.0, that is, positive on the dayside and negative on the nightside. Then the further increase of the R2-FAC intensity causes the reversal of the electric field direction, which takes place between I_{R2}/I_{R1} = 0.7 and I_{R2}/I_{R1} = 0.8. The amplitude of the reversed electric field increases with increasing I_{R2}/I_{R1} from 0.8 to 1.3.

[40] The effect of R2-FAC on the higher latitude region is shown in Figure 3b. The local peaks seen in the high latitude

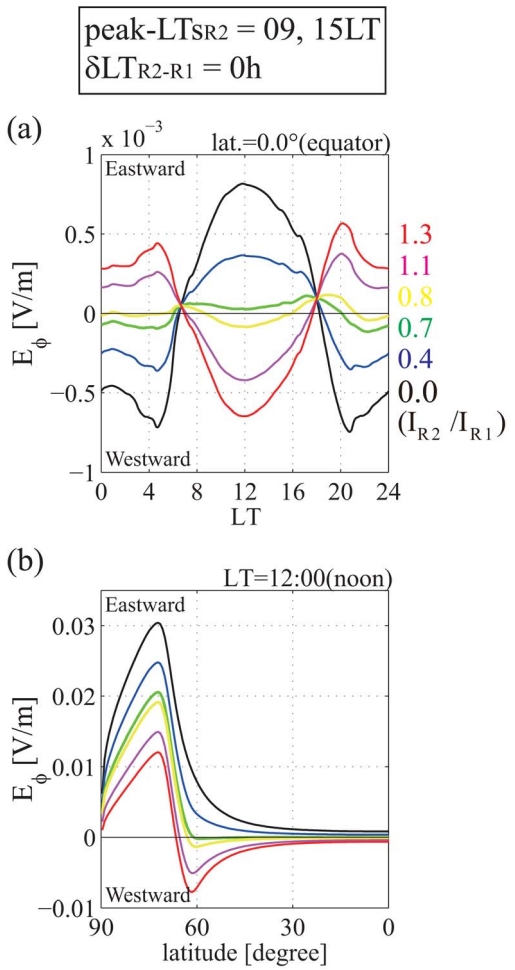

Figure 3. (a) Local time profiles of the longitudinal electric field component, E_φ, along the equator and (b) latitudinal profiles along the noon meridian, which we extracted from two-dimensional patterns shown in Figure 2. E_φ is positive eastward. Horizontal axis in Figure 3a is taken from 00:00LT to 24:00LT and the horizontal axis in Figure 3a is taken from the north pole (90.0°) to the equator (0.0°). Black, blue, green, yellow, magenta, and red colors represent the cases with I_{R2}/I_{R1} of 0.0, 0.4, 0.7, 0.8, 1.1, and 1.3, corresponding to Figures 2a′–2f′, respectively.

region correspond to the concentrated equi-potential lines in Figures 2a′–2f′, being formed just around the source currents. In the case with $I_{R2}/I_{R1} = 0.0$, the latitudinal decay seen on the equatorward side of the peak is a simple geometrical effect, that is, the electric field decreases with the distance from the source current. The electric field is directed eastward in the dayside region from the pole to the equator.

[41] This simplified profile is gradually deformed as R2-FAC becomes more intense. As for the cases with I_{R2}/I_{R1} = 0.4 and 0.7, the peak value is weakened and the slope in the equatorward side of the peak is steepened relative to the case with no R2-FAC, although E_φ is still eastward from the pole to the equator. The sharp spatial decrease is due to R2-FAC imposed just on the equatorward side, which has the polarity opposite to R1-FAC. The increase of R2-FAC leads to the formation of the negative peak and the reversal of electric field in the mid latitude to the equator. The westward peak can be seen for $I_{R2}/I_{R1} = 0.8$, whereas for the smaller values of I_{R2}/I_{R1} the effect of R2-FAC appears to be only the steepening of the latitudinal decrease of the eastward electric field. As I_{R2}/I_{R1} increases from 0.8 the eastward field is weakened and the westward field is intensified. For I_{R2}/I_{R1} = 1.3 the peak value of westward field by R2-FAC becomes comparable to that of the eastward field by R1-FAC.

[42] The value of E_φ at the noon equator (E_{φ,eq_noon}) versus I_{R2}/I_{R1} is shown in Figure 4. We can see from Figure 4 that the change of E_{φ,eq_noon} from eastward to westward is nearly in inverse proportion to the increase of I_{R2}/I_{R1}, with the crossing point between I_{R2}/I_{R1} of 0.7 and 0.8. It is concluded from Figures 2, 3, and 4 that the ionosphere shifts from undershielding condition to overshielding condition between I_{R2}/I_{R1} of 0.7 and 0.8, under the conductivity and FACs distribution used here.

3.3. Dependence on the Spatial Distribution of R2-FAC

[43] Next we investigate how the location of R2-FAC affects the ionospheric electric field. We change the peak local times of R2-FAC toward the nightside. The intensity is also changed in the same way as we did in the previous section. Hereafter, we refer to "the peak local times of R2-FAC" as "peak-LTs_{R2}" and to "the local time deference between the R1 and R2-FAC peaks" as "$\delta LT_{R2\text{-}R1}$," respectively.

[44] The obtained potential patterns are summarized in Figure 5. The format of each panel is the same as that of Figure 2. From the left to the right, peak-LTs_{R2} move toward the nightside with an increment of one hour; peak-LTs_{R2} are 09:00 and 15:00 in the most left column ($\delta LT_{R2\text{-}R1}$ = 0 h, showing the same data with Figure 2) and 06:00 and 18:00 ($\delta LT_{R2\text{-}R1}$ = 3 h, purely dawn and dusk) in the most right column. The FAC distributions with I_{R2}/I_{R1} of 1.3 are shown in the upper row for the purpose of reference. The corresponding results with I_{R2}/I_{R1} of 0.5, 1.0, and 1.3 are shown in the second, third, and bottom rows respectively.

[45] For a given I_{R2}/I_{R1}, the potential pattern is highly deformed as peak-LTs_{R2} move toward the nightside. In the cases with $I_{R2}/I_{R1} = 1.0$, we can recognize in Figure 5b″ the

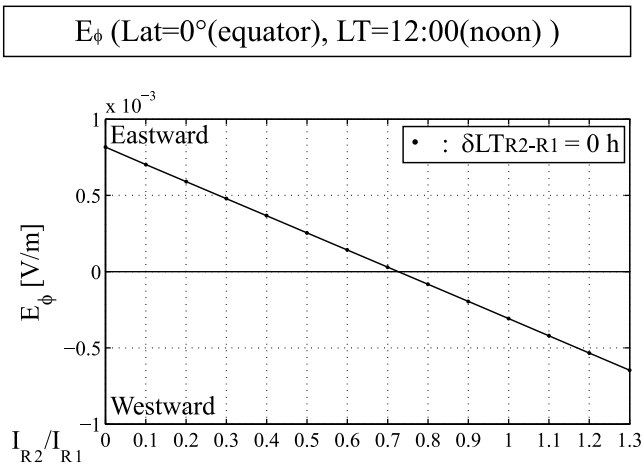

Figure 4. Value of the longitudinal electric field component (E_φ) at the noon equator versus I_{R2}/I_{R1} (the ratio of current intensities of R2 and R1-FACs).

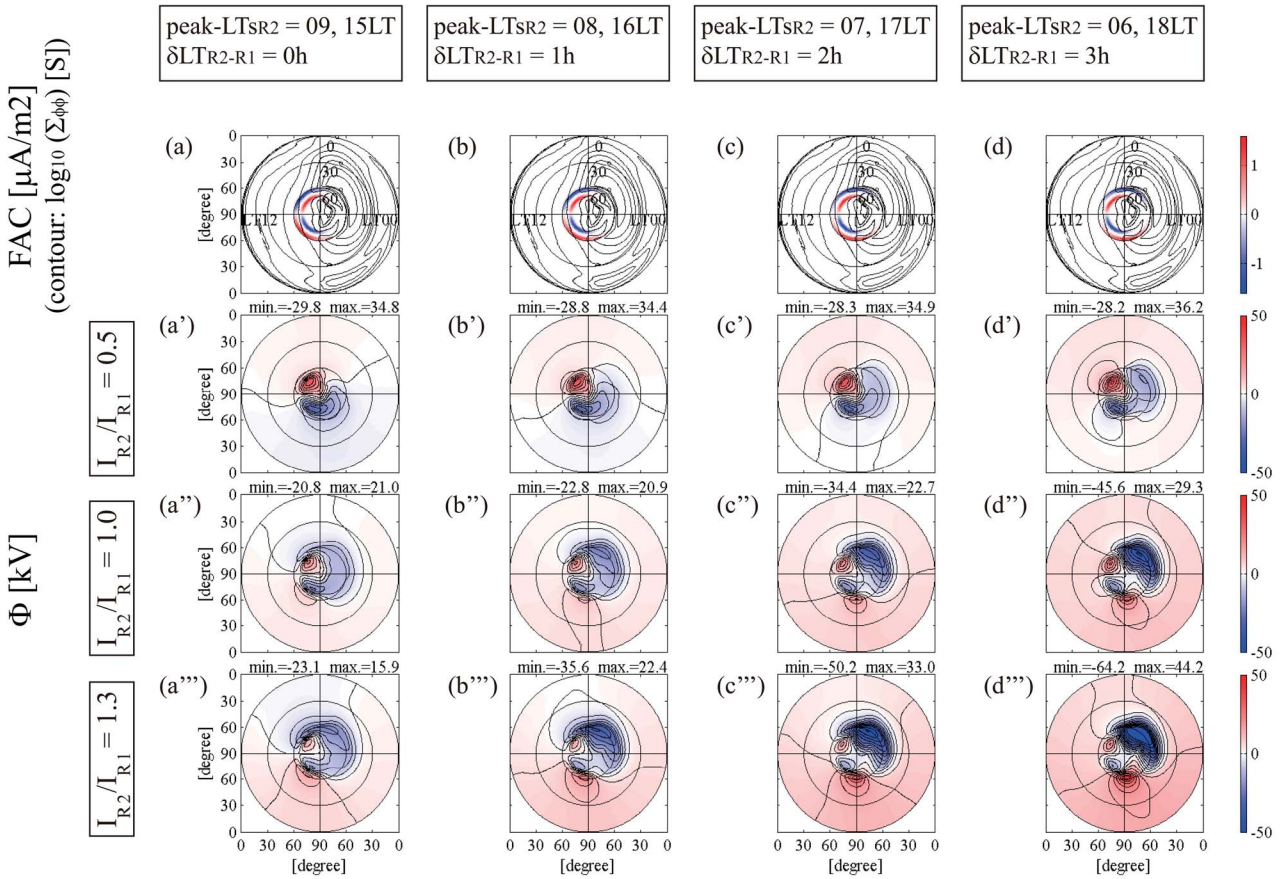

Figure 5. Potential pattern variations with I_{R2}/I_{R1} and peak-LTs_{R2} (the peak local times of R2-FAC). Each panel is displayed in the same format as Figure 2. From left to right, the peak local times of R2-FAC are moved toward the nightside from 09:00 and 15:00 (equals to that of R1-FAC, the same as in section 3.2) to 06:00 and 18:00 (purely dawn and dusk) with an increment of one hour. (a–d) The FAC distributions with I_{R2}/I_{R1} of 1.3 are shown for the purpose of reference. Shown are the results with I_{R2}/I_{R1} of (a′–d′) 0.5, (a″–d″) 1.0, and (a‴–d‴) 1.3.

electric potential due to R2-FAC, which is not clear in Figure 5a″. The R2-potential becomes more noticeable and significant as the peak-LTs_{R2} move toward nightside in Figures 5c″ and 5d″. In the cases with I_{R2}/I_{R1} = 1.3, the R2-potential becomes much stronger and exceeds that of R1-FAC largely in Figures 5c‴ and 5d‴. This tendency is understood by considering the relationship among the current density, conductivity, and electric field. With the same current density, the electric field should become larger in the region of lower conductivity and become smaller in the region of higher conductivity, satisfying the current continuity. Because the ionospheric conductivity is smaller in the nightside than in the dayside, R2-FAC generates the electric field more effectively as it shifts toward the nightside.

[46] The displacement of R2-FAC toward the nightside has another effect on the ionosphere. The clear examples are the cases with I_{R2}/I_{R1} = 1.3. When R1 and R2-FACs have their peaks at the same local time, the electric potential due to R1-FAC are mostly confined in the polar region because of R2-FAC imposed just on the equatorward side (Figure 5a‴). The confinement is partially broken around noon as R2-FAC moves toward the nightside (Figures 5b‴, 5c‴, and 5d‴). As the result, the R1-potential gradually intrudes equatorward through the R2-potential, whereas the R2-potential itself is significantly larger than that of R1-FAC in other local-time sectors. The same tendency can be also found in the cases with I_{R2}/I_{R1} = 1.0. In summary we found two effects of the R2-FAC displacement toward the nightside. That is, the R2-potential becomes clear and significant away from the noon sector, and the shielding effect weakens around noon.

[47] Figure 6 shows the local time and latitudinal profiles of the longitudinal electric field component, E_φ. The formats are the same as in Figure 3. From the left to right, peak-LTs_{R2} are moved toward the nightside, as the same as Figure 5. Figures 6a and 6e show the same data with Figure 3 (peak-LTs_{R2} of 09:00 and 15:00, $\delta LT_{R2\text{-}R1}$ = 0 h). The black line in each panel, which represent the case with I_{R2}/I_{R1} = 0.0 (with no R2-FAC), is the same as shown in the corresponding panel of Figure 3. The aforementioned points can be easily reconfirmed in this figure, that is, as R2-FAC moves toward the nightside, the R2-potential becomes clear and significant away from the noon sector, and the shielding effect weakens around noon.

[48] The local time profiles basically show the bipolar patterns similarly to Figure 3, but some differences can be found. Whereas the reversal of the electric field direction is

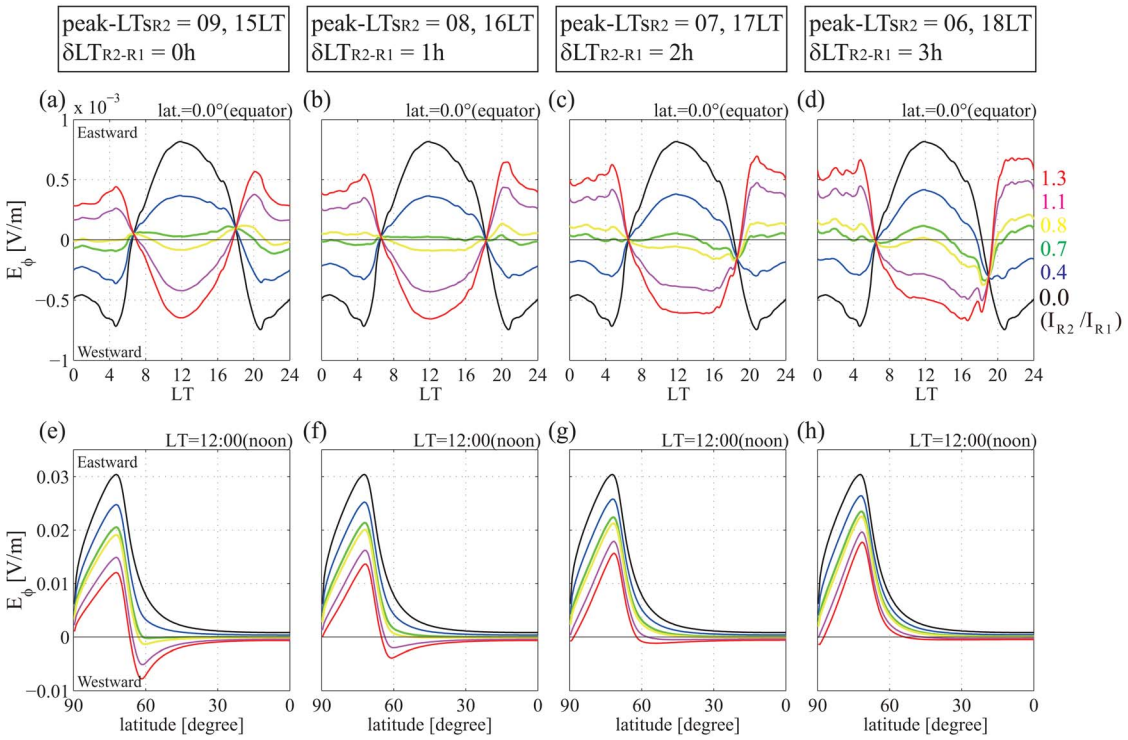

Figure 6. (a–d) Local time profiles of the longitudinal electric field component, E_φ, along the equator and (e–h) latitudinal profiles along the noon meridian. Formats are the same as in Figure 3; E_φ is positive eastward. Horizontal axis ranges from 00:00LT to 24:00LT (Figures 6a–6d) and from the north pole (90.0°) to the equator (0.0°) (Figures 6e–6h). Black, blue, green, yellow, magenta, and red colors represent the cases with I_{R2}/I_{R1} of 0.0, 0.4, 0.7, 0.8, 1.1, and 1.3. From left to right, peak-LTs_{R2} (the peak local times of R2-FAC) are moved toward the nightside from 09:00 and 15:00 (equals to that of R1-FAC, the same as in Figure 3) to 06:00 and 18:00 (purely dawn and dusk) with an increment of one hour, as the same as Figure 5.

between green and yellow lines (I_{R2}/I_{R1} of 0.7 and 0.8) in Figure 6a, it partly takes place between blue and green lines (I_{R2}/I_{R1} of 0.4 and 0.7) in Figures 6b, 6c, and 6d. Besides, after the sign reversal, the local peaks of electric field increases in magnitude both in the dayside and nightside as the plot moves from the left to right. These features indicate that the R2-sense electric field becomes stronger as peak-LTs_{R2} move toward the nightside even for the same I_{R2}/I_{R1}.

[49] In addition an interesting feature can be seen around noon. In Figure 6c, green, yellow, magenta, and red lines are slightly elevated around noon from the levels expected from outside of the noon sector. This deformation can be attributed to the partial penetration of the R1-potential, which seems in Figure 5 to gradually intrude equatorward through the weakened shielding layer as peak-LTs_{R2} move toward the nightside. This feature becomes more significant in Figure 6d, indicating that the magnitude of the shielding decreases in the dayside and the R1-potentail penetrates to the low latitude region more and more as R2-FAC moves toward the nightside. The dawn-dusk asymmetry seen in this longitudinal profile is considered to reflect the dawn-dusk asymmetry of the potential structure extending from the polar region, which is partly due to the dawn-dusk asymmetry of conductivity distribution itself and is partly due to the non-uniformity of the conductivity across the day-night terminators [e.g., *Atkinson and Hutchison*, 1978], which can arise irrespective of the dawn-dusk symmetry. The details, however, is beyond the scope of the present study.

[50] The deformation in the latitudinal profile is understood in detail from Figures 6e–6h. We confirmed in the previous section that R2-FAC causes the formation of the negative peak and the reversal of the electric field in the mid latitude to the equator, steepening the slope on the equatorward side of the positive peak by R1-FAC (Figure 3b, the same as Figure 6e). This is the case in the result with $\delta LT_{R2\text{-}R1}$ = 0 h. The change of peak-LTs_{R2} toward the nightside enhances the effect of R1-FAC relative to that of R2-FAC. From Figures 6e–6h, the equatorward decay of positive peak is moderated and the negative peak is gradually attenuated. Finally in Figure 6h the negative peak is not obvious. At the same time the latitudinal range of negative E_φ becomes narrower and moves equatorward. Conversely, the poleward decay of the positive peak is steepened and in some cases E_φ changes its sign from positive to negative. The deformation in the equatorward side of the positive peak is due to the extension of the R1-potential and that of the poleward side is due to the R2-potential that is intensified and one-sided to the nightside (see Figures 5b‴–5d‴).

[51] The effects of the displacement of R2-FAC toward the nightside are summarized as; The R2-potential is effectively generated with relatively small current intensity (I_{R2}/I_{R1}) but

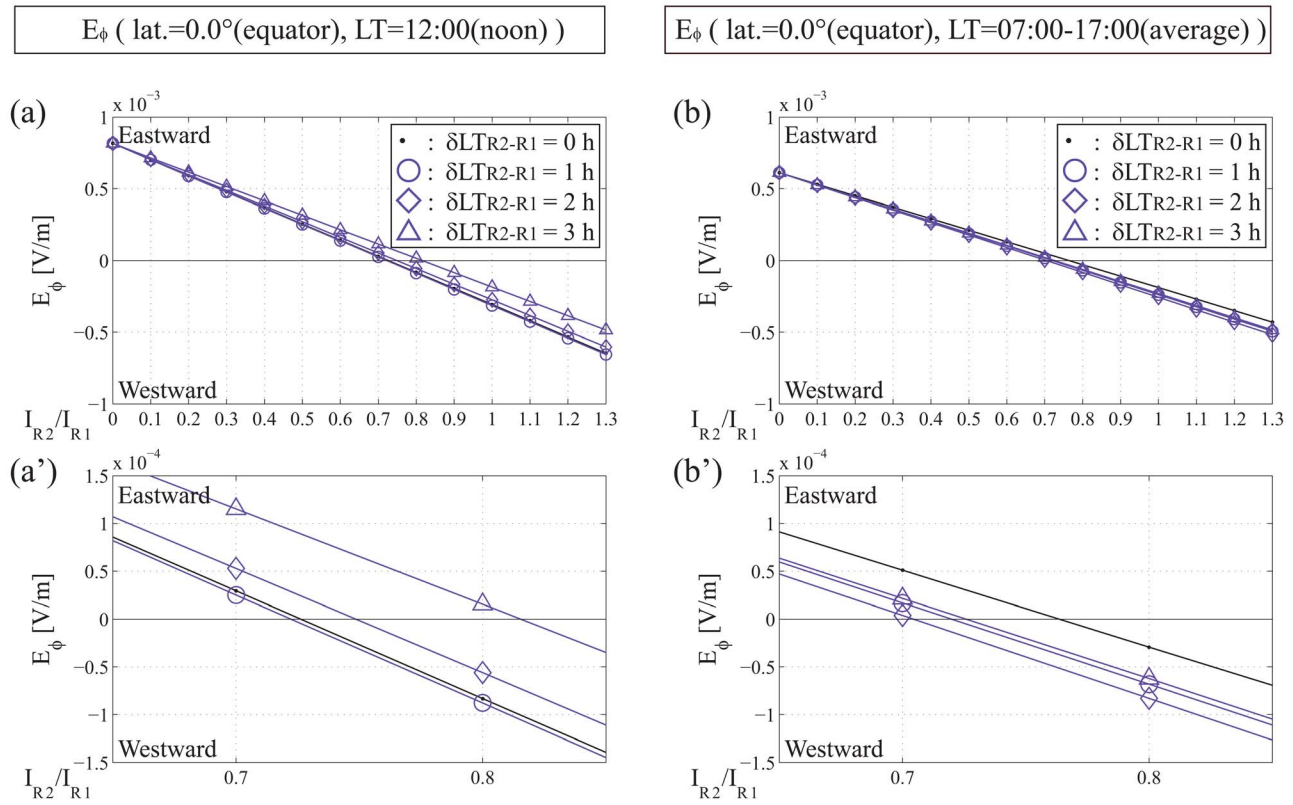

Figure 7. Summary of calculation results. (a) E_φ at the noon equator (E_{φ,eq_noon}) and (b) average of E_φ in the local time sector of 07:00–17:00 (E_{φ,day_ave}) versus I_{R2}/I_{R1} (the ratio of current intensities of R2 and R1-FACs). Enlargement of (a′) Figure 7a around $I_{R2}/I_{R1} = 0.7 \sim 0.8$ and (b′) Figure 7b. Black points and lines show the data with peak-LTs_{R2} of 09:00 and 15:00 ($\delta LT_{R2\text{-}R1}$ = 0 h, equal to those of R1-FAC). Purple marks and lines show the data with shifted R2-FAC; circles, diamonds, and triangle show the data with peak-LTs_{R2} of 08:00 and 16:00LT ($\delta LT_{R2\text{-}R1}$ = 1 h), 07:00 and 17:00LT ($\delta LT_{R2\text{-}R1}$ = 2 h), and 06:00 and 18:00LT ($\delta LT_{R2\text{-}R1}$ = 3 h).

its distribution is skewed to the nightside and the shielding effect is partially weakened around noon.

[52] We summarize all of the calculation results in Figure 7. Figure 7a shows E_φ at the noon equator (E_{φ,eq_noon}) versus I_{R2}/I_{R1}, in the same way as Figure 4. Figure 7b shows the average of E_φ in the local time sector of 07:00–17:00 (E_{φ,day_ave}) versus I_{R2}/I_{R1}. The black points and lines again show the data with peak-LTs_{R2} of 09:00 and 15:00 ($\delta LT_{R2\text{-}R1}$ = 0 h, equal to those of R1-FAC). The data with shifted R2-FAC are shown by the purple marks and lines; the circles, diamonds, and triangle show the data with peak-LTs_{R2} of 08:00 and 16:00LT ($\delta LT_{R2\text{-}R1}$ = 1 h), 07:00 and 17:00LT ($\delta LT_{R2\text{-}R1}$ = 2 h), and 06:00 and 18:00LT ($\delta LT_{R2\text{-}R1}$ = 3 h), respectively. Figures 7a′ and 7b′ enlarge Figures 7a and 7b around $I_{R2}/I_{R1} = 0.7$ and $I_{R2}/I_{R1} = 0.8$.

[53] Relative to the case of $\delta LT_{R2\text{-}R1}$ = 0 h, the negative slope of E_{φ,eq_noon} profile is not so changed in cases with $\delta LT_{R2\text{-}R1}$ = 1 h, but it is moderated in cases with $\delta LT_{R2\text{-}R1}$of 2 and 3 h (Figures 7a and 7a′). On the other hand, the negative slope of E_{φ,day_ave} is steepened with the increase of $\delta LT_{R2\text{-}R1}$ although it is slightly moderated in the cases with $\delta LT_{R2\text{-}R1}$ = 3 h (Figures 7b and 7b′). These features demonstrate the R1 and R2-combined effect mentioned above, that is, along with the shift of R2-FAC toward the nightside, the R2-FAC electric field is created efficiently even with relatively small I_{R2}/I_{R1} (Figures 7b and 7b′), but, at the same time, the dayside low latitude ionosphere includes the structure due to the equatorward extension of the R1-potential (Figures 7a and 7a′).

[54] Finally, we summarize the value of I_{R2}/I_{R1}, at which the ionosphere turns from undershielding to overshielding. In most of all $\delta LT_{R2\text{-}R1}$ cases, the turning point is between $I_{R2}/I_{R1} = 0.7$ and 0.8, although there is a small difference depending on whether the estimation is made from the electric field at noon or from the average electric field over the entire dayside.

4. Discussion

4.1. Completeness of Overshielding: Complete Overshielding and Incomplete Overshielding

[55] The overshielding is an example of the global ionospheric disturbances of the solar wind-magnetospheric origin, and its development can be attributed to the difference in the response time between R1 (convection electric field) and R2- (shielding electric field) FACs. The present study does not address the solar wind-magnetospheric processes but it is concerned with the characteristics of the FACs that lead to the overshielding, such as their intensities and locations.

[56] The present calculation produces the ionospheric electric field pattern in terms of the development of R2-FAC. In some cases with intense R2-FACs, the electric field in the low latitude region changes from the R1-sense (convection electric field) to the R2-sense (shielding electric field). In the dayside equatorial region, the magnitude of the reversed westward electric field reaches 0.2∼0.6 [mV/m]. These features are in a good agreement with the typical observations of the overshielding [e.g., *Gonzales et al.*, 1979; *Kelley et al.*, 1979; *Spiro et al.*, 1988].

[57] However, the present results show various patterns that are not simply classified into the undershielding (R1-dominated condition) or overshielding (R2-dominated condition) and those patterns are primarily determined by the relative locations of R1 and R2-FACs. In the calculation results with finite $\delta LT_{R2\text{-}R1}$ (the local time deference between the R1 and R2-FAC peaks) we found that the R1 electric field extends to the equatorial region in some local time sectors and the overshielding signature locally disappears (Figures 5 and 6 in section 3.3).

[58] These results strongly suggest that the actual ionosphere cannot be unambiguously classified as either undershielding or overshielding. In order to describe more accurately the ionospheric condition, we suggest new classification terms, that is, "complete-overshielding" and "incomplete-overshielding." Here we define the complete-overshielding as the situation that the overall ionosphere on the equatorward side of the auroral region is dominated by the R2-sense electric field, which is the same as the original and strict definition of overshielding. The incomplete-overshielding refers to the situation in which the ionosphere is locally but not globally dominated by the R2-sense electric field.

[59] From the observational point of view, the electric field reversal to the R2-sense indicates that the R2-electric field dominates the R1-electric field at that specific observational site, but it does not tell if the observed R2-sense electric field is global or not. In other words, the single-point observation does not discriminate whether the overall ionospheric electric field pattern is incomplete-overshielding or the complete-overshielding.

[60] In the past the occurrence of the overshielding has been addressed very often based on observations in limited local time and latitudinal ranges. Therefore, we suggest that the observations that were interpreted as overshielding may need to be reexamined in terms of the completeness of the shielding status. For example, *Hashimoto et al.* [2011, Figure 12a] showed that the numbers of overshielding events during substorms distributed mostly in the afternoon sector with its occurrence peak around late afternoon. They suggested that R2-FAC is well developed in the evening side. However, before discussing the "spatial dependence of the occurrence of overshielding," the signature of overshielding should be detected everywhere if the event is really the complete one. Inversely, we should call such events as the overshielding. Another example is the discussion on the relationship between the occurrence of overshielding and the external condition. *Wei et al.* [2011] reported an example that the northward turning of IMF-Bz does not lead to the subsequent overshielding, contrary to the usual expectation. That event is certainly not a complete-overshielding but there is a possibility that it is an example for the incomplete-overshielding.

[61] In closing the above discussion, we suggest that the ionospheric condition, undershielding, incomplete-overshielding, or complete-overshielding, should be cautiously identified by observing the overall ionosphere as much as possible and this terminology should be used carefully. In practice, however, it is sometimes difficult to observe the ionosphere with the sufficient coverage. In such a case, the reversal of the electric field at the noon equator may be a good indicator of the overshielding because in such a condition the ionosphere is totally dominated by the R2-electric field even if it partially includes the structure due to the R1-electric field. We suggest that, in order to diagnose not only the shielding status (i.e., overshielding or undershielding) but also the potential distribution, we need to measure ionospheric electric fields on the day side at least six locations, more specifically, we need three equator- middle latitude pairs at the dawn, noon, and dusk meridian. The latitudinal pair is necessary to diagnose whether the partial structure exist at each meridian. Three meridional pairs are necessary to address whether the partial structure is that of the bipolar structure, such as a dawn-dusk asymmetry, or that of the embedded structure, as seen in the present calculation (Figure 5).

4.2. Ultimate Factor in Determining the Shielding Status

[62] The northward turning of IMF-Bz after a prolonged southward period itself is a typical signature with which the occurrence of overshielding has been mostly investigated. However, this is not necessarily the exclusive cause of either the complete or incomplete-overshielding because there are various intermediate magnetospheric and ionospheric processes that occur responding to the solar wind/IMF changes before the convection electric field and shielding electric field are established, and the shielding status is ultimately determined by the balance between these electric fields. In fact, whether the northward turning is a necessary and sufficient condition for the overshielding is currently the subject of a controversy. In addition to an example of the northward turning without subsequent overshielding [*Wei et al.*, 2011] mentioned above (of course, the shielding status should be determined carefully), the overshielding accompanied by no typical solar wind change is reported, for example, by *Fejer et al.* [2007] and *Ebihara et al.* [2008]. There are many possible factors to take into account for these cases such as the polar cap contraction [*Ebihara et al.*, 2008; *Kikuchi et al.*, 2008], the sharpness of the northward turning and the preconditioning of the magnetosphere [*Wei et al.*, 2011]. As an extension to these considerations, the present study suggests that the relative intensity and location of R1 and R2-FACs, which are determined as a consequence of these magnetospheric and ionospheric processes, may play a crucial role in determining the shielding status.

4.3. Estimation of the FACs Efficiency

[63] In the present calculation, the turning point, at which the ionosphere changes from undershielding to overshielding, is between I_{R2}/I_{R1} (the ratio of current intensities of R2 and R1-FACs) = 0.7 and 0.8. The first important point the

result indicates is that the overshielding can occur even if R2-FAC does not exceed R1-FAC. The second important point is that the ionosphere is in a state of delicate balance between R1 and R2-FACs when $I_{R2}/I_{R1} = 0.7 \sim 0.8$. Interestingly, the obtained turning point of I_{R2}/I_{R1} coincides with the statistical distribution of FACs during moderately disturbed period ($2- \leq Kp \leq 4+$) provided by *Iijima and Potemra* [1976], in which I_{R2}/I_{R1} is 0.80 in the morning sector and is 0.83 in the evening sector (see their Table 1). However, the present results need to be addressed carefully when quantitatively comparing with observations because the results depend on the assumed conductivity and FAC distribution. In fact, a simple comparison between the present result and the I_{R2}/I_{R1} ratio reported by *Iijima and Potemra* [1976] suggests that the overshielding occurs at fifty percent of time. However, such a high occurrence frequency of the overshielding cannot be supported observationally.

[64] This apparent discrepancy can be explained in terms of the consistency between FACs and conductivity distribution. In the present study, we adjusted the latitudinal distribution of R1 and R2-FACs to the conductivity enhancement representing the auroral region. But our method is not perfect because the development of FACs and that of the conductivity are closely related to each other. This deductive aspect of the consistency between FACs and conductivity will be discussed later. Here we discuss the inductive aspect of the relationship between FACs and conductivity distributions.

[65] There are two possible factors responsible for the error in the estimation of the FACs efficiency. Here "the FACs efficiency" refers to the FAC effect on the ionospheric electric field. One is the spatial distribution of FACs itself. The other is the conductivity in the auroral region, which largely controls the FACs efficiency.

[66] First we consider the former factor. In this study, R1-FAC is distributed by refereeing an empirical distribution [*Hori et al.*, 2009], with its peaks at 09:00 and 15:00 in the local time. On the other hand, R2-FAC is given somewhat arbitrarily, with its distribution symmetrical to R1-FAC and its peak local times from 09:00 and 15:00 to 06:00 and 18:00, because the goal of the present research is to provide the basic understanding of the R2-FAC effect relative to the fixed conductivity and R1-FAC rather than reproducing actual phenomena. According to *Iijima and Potemra* [1976, Figure 3b], R2-FAC has the largest current densities in the nightside region, where the effect of the source current is likely more amplified than in the present calculation due to lower conductivities. If we simply apply the R2-FAC distribution by *Iijima and Potemra* [1976], the calculation will show the lower turning point of I_{R2}/I_{R1} and therefore it follows that the overshielding should occur very frequently with observational I_{R2}/I_{R1} by *Iijima and Potemra* [1976]. This consideration worsens the estimation of the R2-FAC efficiency.

[67] Next we consider the later factor. Recently, *Aksnes et al.* [2002] derived the conductivity distribution in the high latitude region during a substorm. They pointed out that the Hall conductivity is underestimated in existing statistical models, in which the model by *Hardy et al.* [1987] used in this study is included. The difference in the conductivity estimation between *Aksnes et al.* [2002] and existing models is primary related to the coverage of electron energy range responsible for the conductivity. *Aksnes et al.* [2002] cover the whole electron energy range by combining data from the Polar Ionospheric X-ray Imager (PIXIE) and the Ultraviolet Imager (UVI) on board the Polar satellite. Underestimation in the conductivity results in the overestimation of the FACs efficiency due to the relationship between the source currents, conductivity, and electric field. The largest current densities in the nightside region of R2-FAC by *Iijima and Potemra* [1976] are mainly related to the geomagnetic activities including substorms. During such active times, the conductivity will actually be amplified than that of the statistical models preceding *Aksnes et al.* [2002]. Summing up these considerations, the effect of the nightside R2-FAC on the shielding status should be suppressed with the realistic conductivity distribution. Then this consideration does not worsen the estimation of the R2-FAC efficiency.

[68] The above discussion is mainly devoted to R2-FAC, but the same discussion is also applied to R1-FACs. If the observational and global distribution of either of FACs or conductivity is available, it would be possible that we derive the distribution of the other through the comparison between the observed electric field and calculated one. This is one of the inductive ways to improve the FACs and conductivity distributions.

[69] Although we mention above the difference between the R2-FAC distribution by *Iijima and Potemra* [1976] (the largest current densities in the nightside region) and that of ours (the peak current densities at local times from 09:00 and 15:00 to 06:00 and 18:00), finally we would like to suggest that R2-FAC does not necessarily have its peaks on the night side even during active times especially when the R2-FAC is driven by global convection. According to the FACs distribution provided by *Juusola et al.* [2007], R2-FAC is mainly distributed on the day side rather than on the night side. Its peak is not located at the nightside. The discrepancy between *Iijima and Potemra* [1976] and *Juusola et al.* [2007] can be explained by separately considering non-storm time substorms and storm-time convection enhancements. During substorms, the FAC is generated in association with activities in the inner edge of the plasma sheet such as injection and depolarization [e.g., *Rostoker et al.*, 1980]. This substorm-associated FAC is superposed on the existing "large-scale (associated with the large-scale convection)" R1 and R2-FACs resulting in the apparent nightside peaks in the global FACs distribution. Actually, nightside maximum of R2-FAC by *Iijima and Potemra* [1976] can be attributed mainly to this substorm associated process (see the sixth item in their summary). In contrast, if the R2 current, therefore the ring current, is driven by enhanced global convection such as expected for the storm main phase, the tailward and sunward convection is driven by large-scale electric field associated with R1 and R2 pair. This is the case we consider in the present study. In order to maintain the sunward convection electric field, the R2 should be distributed in the same local time sector as the strong R1 current on the day side. Otherwise, the R1-origin electric field would penetrate deeply into the lower latitude region, which, however, has not been supported by observation [e.g., *Goldstein*, 2006]. The "partial" imbalance between R1 and R2-FACs may occur more frequently during substorms rather than during storms. The observation by *Hashimoto*

et al. [2011], discussed in section 4.1, may be a good example for the former. Obviously this issue needs to be addressed more carefully with observations, which is, however, beyond the scope of the present study.

4.4. Limitation and Applicability of the Model

[70] Next we would like to address the limitation of our approach in terms of its applicable timescale. One important reminder is that the calculation results do not represent anything more than steady state conditions that the ionosphere would reach with an imposed source current and an assumed ionospheric conductivity distribution because our model solves the Poisson type equation. Therefore, the calculation results do not necessarily represent ionospheric snapshots of time-varying phenomena. However, the calculation results should still be useful for discussing transient ionospheric conditions if the associated time scales are longer than a certain relaxation time. Here we would like to make two points. The first point is the time it takes for the electric field imposed by source currents to prevail throughout the ionosphere. *Kikuchi and Araki* [1979] theoretically proposed the instantaneous transmission of the polar electric field to the equator by using an Earth-ionosphere waveguide model. From the geomagnetic field observations, it is reported that the disturbances originated from the polar region seems to be transmitted nearly instantaneously to the low-latitude and equatorial regions within the sampling resolution (about ten seconds) [e.g., *Kikuchi et al.*, 1996]. We can therefore assume that the required time relevant to this point is comparable to their sampling resolution at the maximum estimate. The second point is the time it takes for the ionosphere to reach a steady state, assimilating itself to the mapped electric field. According to *Yoshikawa and Itonaga* [1996, 2000], the FAC and ionospheric rotation Hall current are inductively coupled through the multistep Hall effect. A characteristic time scale to reach the steady state depends on the horizontal scale length of FAC distribution and amplitude of ionospheric conductivity, which becomes about several tens of seconds at auroral zone [*Yoshikawa*, 2002a, 2002b]. Considering these two points, we conclude that calculation results are applicable for the phenomena, the timescales of which are longer than a few tens of seconds.

[71] The other important reminder is that the dynamics of the neutral wind has not been considered in this study. Even when the electric field of the magnetospheric origin is suddenly decreased, the ion convection can be maintained by the neutral wind inertia. This effect is generally described by "fly-wheel effect" [*Banks*, 1972; *Richmond and Matsushita*, 1975]. Energy input from the magnetosphere to the thermosphere, which usually takes place in the form of the joule heating in the auroral zone, sometimes alters the wind field. Consequently, the neutral wind dynamo field can be changed. During geomagnetic active times, this effect becomes significant and is known as "disturbance dynamo" [e.g., *Blanc and Richmond*, 1980]. So we should be careful when we deal with phenomena, time scales of which are longer than the system time of the neutral wind dynamics. For such phenomena, the effects of the neutral wind can be important [*Rees and Fuller-Rowell*, 1989; *Ridley et al.*, 2003; *Förster et al.*, 2011]. For example, during storm recovery phases, the reversal of the electric field in the dayside equatorial region sometimes persists for a long time. The long-lasting component (duration time of many hours) is thought to be causally related to the neutral wind dynamics, the effect of which is usually described by above mentioned "disturbance dynamo" [e.g., *Blanc and Richmond*, 1980]. The short-lasting component (several tens of minutes) is attributed to the overshielding, with which the present study is concerned.

4.5. The Magnetosphere-Inner Magnetosphere Coupling Through the Ionosphere

[72] Recently some attempts were made to couple magnetosphere MHD models with inner-magnetosphere models [e.g., *De Zeeuw et al.*, 2004]. A focus has been placed on the self-consistent connection of these two types of models at the interface in the magnetosphere. However, it still remains to be understood how the outer magnetosphere and inner magnetosphere interact each other through the interface at the ionospheric altitude. In principle, the MHD models do not accurately reproduce R2-FAC. On the other hand, the inner-magnetosphere models [e.g., *Fok et al.*, 2001; *Toffoletto et al.*, 2003] require at the poleward boundary the polar cap potential or R1-FAC, which are usually distributed empirically or semi-empirically. The calculations of the pole-to-pole ionosphere performed in this study show that the ionospheric electric field is significantly affected by the pair of R1 and R2 FACs. The mid latitude to the equatorial ionosphere shows complex structures of the R1 and R2-electric fields in some cases. The electric field in the polar region is also substantially distorted by the intensification of R2-FAC (Figure 5, in section 3.3). We suggest that it is necessary to take into account in the future modeling studies the viewpoint of the magnetosphere-inner magnetosphere coupling through the ionosphere.

4.6. Future Improvement Associated With the M-I Coupling

[73] Finally we would like to address the FAC and ionospheric conductivity, which are the essential elements of the M-I coupling. In a local aspect, the development of the FAC and that of the conductivity are intrinsically related to each other. In a global aspect, the ultimate distribution of the FAC and the ionospheric conductivity are determined as the consequence of the self-consistency in the magnetosphere-ionosphere coupled system.

[74] In order to simplify the problem, we fixed the conductivity and R1-FAC distributions in both the intensity and spatial distribution. The problem seems to be deduced to the issue of a R2-FAC control over the shielding electric field, but we do not separate completely (still have mixture of) the FAC effect and conductivity effect. We independently set the FAC and the ionospheric conductivity because there is still no established way to give their self-consistent and global distribution.

[75] Recently *Yoshikawa et al.* [2011b] formulate the evolution of ionospheric conductivity in the framework of 3D M-I coupling, which is more general than the previous studies and is not limited to certain geometries, current components or interaction modes between the ionosphere and magnetosphere. It is therefore better suited for describing the self-organized M-I coupling system, which evolves with current systems, conductivity, and magnetospheric processes

interacting with each other. These problems related to the fundamentals of the M-I coupling will be continuously reconsidered in future works.

5. Summary

[76] In order to provide the knowledge for the relationship between disturbances originating from the solar wind or magnetosphere and the global ionospheric structure, we developed a two-dimensional ionospheric potential solver, GEMSIS-POT. Our model is based on the so-called "thin shell model"; it solves the Ohm's law under the thin shell approximated ionosphere with FACs in the polar region and the height-integrated ionospheric conductivity. Our model covers the pole-to-pole ionosphere without placing any boundary at the equator. The distribution of FACs can be set depending on the objective of the study. These two points are the important extensions from the previous studies. The ionospheric conductivity is calculated as exactly as possible with the MSIS-2000 and IRI-2007 models. As for the ambient magnetic field, the IGRF-2005 reference model or dipole field can be used. The unrealistic enhancement of conductivity in the low latitude region arising inevitably from the thin shell approximation is modified by a method suggested by *Tsunomura* [1999]. The conductivity enhancement in the auroral region is also included.

[77] By using the solver, we investigated how the ionospheric electric field changes from undershielding condition to overshielding condition as the intensity and distribution of R2-FAC changes. In the present calculation we distributed R1-FAC by a Gaussian function referring to an empirical distribution [*Hori et al.*, 2009] with its local time peaks at 09:00 and 15:00LT. We also distributed R2-FAC in the same way. Their peak latitudes are adjusted in such a way that they are confined inside the conductivity enhancements representing the auroral region.

[78] Calculations were performed by changing I_{R2}/I_{R1} (the ratio of current intensities of R2 and R1-FACs) and moving R2-FAC toward the nightside with $\delta LT_{R2\text{-}R1}$ (the local time deference between the R1 and R2-FAC peaks) under the fixed R1-FAC and conductivity distributions. We focused on the value of I_{R2}/I_{R1}, at which the ionosphere turns from undershielding to overshielding, and the electric field pattern changes.

[79] We found that the turning point is between I_{R2}/I_{R1} = 0.7 and 0.8, although there is a small difference depending on whether the estimation is made from the electric field at noon or from the average electric field over the entire dayside.

[80] We also found that the calculation results show complex patterns, depending on $\delta LT_{R2\text{-}R1}$, that cannot be classified into the undershielding or overshielding. As R2-FAC moves toward the nightside, the R2-potential is effectively generated with relatively small I_{R2}/I_{R1}, but the shielding effect is partially weakened around noon because the R2-potential is skewed to the nightside. At the same time the R1-potential intrudes equatorward through the weakened shielding layer around noon. As the result of these R1 and R2-combined effect, the ionosphere includes the structure due to the R1-potential in the dayside low latitude region while the R2-potential dominates in other local-time sectors. We therefore suggest that the overshielding or undershielding should be identified based not only on observations in a limited local time sector but also observations for the overall ionosphere as much as possible. In order to describe more accurately the ionospheric condition, we suggest new classification terms, that is, "complete-overshielding" and "incomplete-overshielding."

[81] **Acknowledgments.** We are deeply grateful to A. Yoshikawa for enlightening comments and discussions based on his profound insight into the Magnetosphere-Ionosphere coupling. We are also very grateful to S. Ohtani for fruitful discussions. S. Oyama is acknowledged for discussion on the derivation of the ionospheric conductivity. This work has been supported by the GEMSIS project of the Solar-Terrestrial Environment Laboratory in Nagoya University.

[82] Robert Lysak thanks the reviewers for their assistance in evaluating this paper.

References

Ahn, B.-H., Y. Kamide, and S.-I. Akasofu (1986), Electrical changes of the polar ionosphere during magnetospheric substorms, *J. Geophys. Res.*, *91*(A5), 5737–5754, doi:10.1029/JA091iA05p05737.

Aksnes, A., J. Stadsnes, J. Bjordal, N. Østgaard, R. R. Vondrak, D. L. Detrick, T. J. Rosenberg, G. A. Germany, and D. Chenette (2002), Instantaneous ionospheric global conductance maps during an isolated substorm, *Ann. Geophys.*, *20*, 1181–1191, doi:10.5194/angeo-20-1181-2002.

Amm, O. (1996), Comment on "A three-dimensional, iterative mapping procedure for the implementation of an ionosphere-magnetosphere anisotropic Ohm's law boundary condition in global magnetohydrodynamic simulations" by Michael L. Goodman, *Ann. Geophys.*, *14*, 773–774.

Araki, T. (1994), A physical model of the geomagnetic sudden commencement, in *Solar Wind Sources of Magnetospheric Ultra-Low-Frequency Waves*, *Geophys. Monogr. Ser*, vol. 81, edited by M. J. Engebreston, K. Takahashi, and M. Scholer, pp. 183–200, AGU, Washington, D. C., doi:10.1029/GM081p0183.

Atkinson, G., and D. Hutchison (1978), Effect of the day night ionospheric conductivity gradient on polar cap convective flow, *J. Geophys. Res.*, *83*(A2), 725–729, doi:10.1029/JA083iA02p00725.

Banks, P. M. (1972), Magnetospheric processes and the behavior of the neutral atmosphere, *Space Res.*, *12*, 1051–1067.

Bilitza, D., and B. W. Reinisch (2008), International Reference Ionosphere 2007: Improvements and new parameters, *Adv. Space Res.*, *42*, 599–609, doi:10.1016/j.asr.2007.07.048.

Birkeland, K. (1908), *The Norwegian Aurora Polaris Expedition 1902–3*, vol. 1, *On the Cause of Magnetic Storms and the Origin of Terrestrial Magnetism*, H. Aschehoug, Christiania, Norway.

Blanc, M., and A. D. Richmond (1980), The ionospheric disturbance dynamo, *J. Geophys. Res.*, *85*(A4), 1669–1686, doi:10.1029/JA085iA04p01669.

Brekke, A., and J. Moen (1993), Observations of high latitude ionospheric conductances, *J. Atmos. Terr. Phys.*, *55*(11–12), 1493–1512, doi:10.1016/0021-9169(93)90126-J.

De Zeeuw, D. L., S. Sazykin, R. A. Wolf, T. I. Gombosi, A. J. Ridley, and G. Tóth (2004), Coupling of a global MHD code and an inner magnetospheric model: Initial results, *J. Geophys. Res.*, *109*, A12219, doi:10.1029/2003JA010366.

Ebihara, Y., and Y. Miyoshi (2011), Dynamic inner magnetosphere: A tutorial and recent advances, in *The Dynamic Magnetosphere*, *IAGA Spec. Sopron Book Ser.*, vol. 3, edited by W. Liu and M. Fujimoto, pp. 145–187, Springer, Dordrecht, Netherlands, doi:10.1007/978-94-007-0501-2_9.

Ebihara, Y., N. Nishitani, T. Kikuchi, T. Ogawa, K. Hosokawa, and M.-C. Fok (2008), Two-dimensional observations of overshielding during a magnetic storm by the Super Dual Auroral Radar Network (SuperDARN) Hokkaido radar, *J. Geophys. Res.*, *113*, A01213, doi:10.1029/2007JA012641.

Fejer, J. A. (1953), Semidiurnal currents and electron drifts in the ionosphere, *J. Atmos. Terr. Phys.*, *4*, 184–203, doi:10.1016/0021-9169(53)90054-3.

Fejer, B. G., C. A. Gonzales, D. T. Farley, M. C. Kelley, and R. Woodman (1979), Equatorial electric fields during magnetically disturbed conditions: 1. The effect of the interplanetary magnetic field, *J. Geophys. Res.*, *84*(A10), 5797–5802, doi:10.1029/JA084iA10p05797.

Fejer, B. G., J. W. Jensen, T. Kikuchi, M. A. Abdu, and J. L. Chau (2007), Equatorial ionospheric electric fields during the November 2004 magnetic storm, *J. Geophys. Res.*, *112*, A10304, doi:10.1029/2007JA012376.

Fok, M.-C., R. A. Wolf, R. W. Spiro, and T. E. Moore (2001), Comprehensive computational model of the Earth's ring current, *J. Geophys. Res.*, *106*(A5), 8417–8424, doi:10.1029/2000JA000235.

Forbes, J. M., and R. S. Lindzen (1976a), Atmospheric solar tides and their electrodynamic effects—I. The global S_q current system, *J. Atmos. Terr. Phys.*, *38*, 897–910, doi:10.1016/0021-9169(76)90073-8.

Forbes, J. M., and R. S. Lindzen (1976b), Atmospheric solar tides and their electrodynamic effects—II. The equatorial electrojet, *J. Atmos. Terr. Phys.*, *38*, 911–920, doi:10.1016/0021-9169(76)90074-X.

Förster, M., S. E. Haaland, and E. Doornbos (2011), Thermospheric vorticity at high geomagnetic latitudes from CHAMP data and its IMF dependence, *Ann. Geophys.*, *29*, 181–186, doi:10.5194/angeo-29-181-2011.

Fujii, R., O. Amm, A. Yoshikawa, A. Ieda, and H. Vanhamäki (2011), Reformulation and energy flow of the Cowling channel, *J. Geophys. Res.*, *116*, A02305, doi:10.1029/2010JA015989.

Goldstein, J. (2006), Plasmasphere response: Tutorial and review of recent imaging results, *Space Sci. Rev.*, *124*(1–4), 203–216, doi:10.1007/s11214-006-9105-y.

Gombosi, T. I., D. L. DeZeeuw, C. P. T. Groth, and K. G. Powell (2000), Magnetospheric configuration for Parker-spiral IMF conditions: Results of a 3D AMR MHD simulation, *Adv. Space Res.*, *26*(1), 139–149, doi:10.1016/S0273-1177(99)01040-6.

Gonzales, C. A., M. C. Kelley, B. G. Fejer, J. F. Vickrey, and R. F. Woodman (1979), Equatorial electric fields during magnetically disturbed conditions: 2. Implications of simultaneous auroral and equatorial measurements, *J. Geophys. Res.*, *84*(A10), 5803–5812, doi:10.1029/JA084iA10p05803.

Hardy, D. A., M. S. Gussenhoven, R. Raistrick, and W. J. McNeil (1987), Statistical and functional representations of the pattern of auroral energy flux, number flux, and conductivity, *J. Geophys. Res.*, *92*(A11), 12,275–12,294, doi:10.1029/JA092iA11p12275.

Harel, M., R. A. Wolf, P. H. Reiff, R. W. Spiro, W. J. Burke, F. J. Rich, and M. Smiddy (1981a), Quantitative simulation of a magnetospheric substorm: 1. Model logic and overview, *J. Geophys. Res.*, *86*(A4), 2217–2241, doi:10.1029/JA086iA04p02217.

Harel, M., R. A. Wolf, R. W. Spiro, P. H. Reiff, C.-K. Chen, W. J. Burke, F. J. Rich, and M. Smiddy (1981b), Quantitative simulation of a magnetospheric substorm: 2. Comparison with observations, *J. Geophys. Res.*, *86*(A4), 2242–2260, doi:10.1029/JA086iA04p02242.

Hashimoto, K. K., T. Kikuchi, S. Watari, and M. A. Abdu (2011), Polar-equatorial ionospheric currents driven by the region 2 field-aligned currents at the onset of substorms, *J. Geophys. Res.*, *116*, A09217, doi:10.1029/2011JA016442.

Hori, T., Y. Ebihara, Y. Hiraki, A. Shinbori, A. Ieda, T. Kikuchi, G. Ueno, T. Higuchi, S. Wing, and S. Ohtani (2009), An empirical field-aligned current model based on the DMSP and DE2 satellites, *Eos Trans. AGU*, *90*(52), Fall Meet. Suppl., Abstract SM51A-1324.

Iijima, T. (2000), Field-aligned currents in geospace: Substance and significance, in *Magnetospheric Current Systems*, *Geophys. Monogr. Ser*, vol. 118, edited by S. Ohtani et al., pp. 107–129, AGU, Washington, D. C., doi:10.1029/GM118p0107.

Iijima, T., and T. A. Potemra (1976), The amplitude distribution of field-aligned currents at northern high latitudes observed by Triad, *J. Geophys. Res.*, *81*(13), 2165–2174, doi:10.1029/JA081i013p02165.

Jaggi, R. K., and R. A. Wolf (1973), Self-consistent calculation of the motion of a sheet of ions in the magnetosphere, *J. Geophys. Res.*, *78*(16), 2852–2866, doi:10.1029/JA078i016p02852.

Janhunen, P. (1998), On the possibility of using an electromagnetic ionosphere in global MHD simulations, *Ann. Geophys.*, *16*, 397–402, doi:10.1007/s00585-998-0397-y.

Juusola, L., O. Amm, K. Kauristie, and A. Viljanen (2007), A model for estimating the relation between the Hall to Pedersen conductance ratio and ground magnetic data derived from CHAMP satellite statistics, *Ann. Geophys.*, *25*, 721–736, doi:10.5194/angeo-25-721-2007.

Kamide, Y., and S. Matsushita (1979a), Simulation studies of ionospheric electric fields and currents in relation to field-aligned currents: 1. Quiet periods, *J. Geophys. Res.*, *84*(A8), 4083–4098, doi:10.1029/JA084iA08p04083.

Kamide, Y., and S. Matsushita (1979b), Simulation studies of ionospheric electric fields and currents in relation to field-aligned currents: 2. Substorms, *J. Geophys. Res.*, *84*(A8), 4099–4115, doi:10.1029/JA084iA08p04099.

Kamide, Y., A. D. Richmond, and S. Matsushita (1981), Estimation of ionospheric electric fields, ionospheric currents, and field-aligned currents from ground magnetic records, *J. Geophys. Res.*, *86*(A2), 801–813, doi:10.1029/JA086iA02p00801.

Kelley, M. C., B. G. Fejer, and C. A. Gonzales (1979), An explanation for anomalous equatorial ionospheric electric fields associated with a northward turning of the interplanetary magnetic field, *Geophys. Res. Lett.*, *6*(4), 301–304, doi:10.1029/GL006i004p00301.

Kikuchi, T., and T. Araki (1979), Horizontal transmission of the polar electric field to the equator, *J. Atmos. Sol. Terr. Phys.*, *41*, 927–936, doi:10.1016/0021-9169(79)90094-1.

Kikuchi, T., H. Lühr, T. Kitamura, O. Saka, and K. Schlegel (1996), Direct penetration of the polar electric field to the equator during a DP 2 event as detected by the auroral and equatorial magnetometer chains and the EISCAT radar, *J. Geophys. Res.*, *101*(A8), 17,161–17,173, doi:10.1029/96JA01299.

Kikuchi, T., H. Lühr, K. Schlegel, H. Tachihara, M. Shinohara, and T.-I. Kitamura (2000), Penetration of auroral electric fields to the equator during a substorm, *J. Geophys. Res.*, *105*(A10), 23,251–23,261, doi:10.1029/2000JA900016.

Kikuchi, T., K. K. Hashimoto, T.-I. Kitamura, H. Tachihara, and B. Fejer (2003), Equatorial counterelectrojets during substorms, *J. Geophys. Res.*, *108*(A11), 1406, doi:10.1029/2003JA009915.

Kikuchi, T., K. K. Hashimoto, and K. Nozaki (2008), Penetration of magnetospheric electric fields to the equator during a geomagnetic storm, *J. Geophys. Res.*, *113*, A06214, doi:10.1029/2007JA012628.

Maeda, H., and K. Maekawa (1973), A numerical study of polar ionospheric currents, *Planet. Space Sci.*, *21*, 1287–1300, doi:10.1016/0032-0633(73)90221-3.

Maeda, H., T. Iyemori, T. Araki, and T. Kamei (1982), New evidence of a meridional current system in the equatorial ionosphere, *Geophys. Res. Lett.*, *9*(4), 337–340, doi:10.1029/GL009i004p00337.

Musmann, G., and E. Seiler (1978), Detection of meridional currents in the equatorial ionosphere, *J. Geophys.*, *44*, 357–372.

Nisbet, J. S., M. J. Miller, and L. A. Carpenter (1978), Currents and electric fields in the ionosphere due to field-aligned auroral currents, *J. Geophys. Res.*, *83*(A6), 2647–2657, doi:10.1029/JA083iA06p02647.

Nishida, A. (1968), Coherence of geomagnetic DP 2 fluctuations with interplanetary magnetic variations, *J. Geophys. Res.*, *73*(17), 5549–5559, doi:10.1029/JA073i017p05549.

Nishida, A., N. Iwasaki, and T. Nagata (1966), The origin of fluctuations in the equatorial electrojet: A new type of geomagnetic variation, *Ann. Geophys.*, *22*, 478–484.

Nopper, R. W., Jr., and R. L. Carovillano (1978), Polar-equatorial coupling during magnetically active periods, *Geophys. Res. Lett.*, *5*(8), 699–702, doi:10.1029/GL005i008p00699.

Peymirat, C., and D. Fontaine (1994), Numerical simulation of magnetospheric convection including the effect of field-aligned currents and electron precipitation, *J. Geophys. Res.*, *99*(A6), 11,155–11,176, doi:10.1029/93JA02546.

Peymirat, C., A. D. Richmond, and A. T. Kobea (2000), Electrodynamic coupling of high and low latitudes: Simulations of shielding/overshielding effects, *J. Geophys. Res.*, *105*(A10), 22,991–23,003, doi:10.1029/2000JA000057.

Picone, J. M., A. E. Hedin, D. P. Drob, and A. C. Aikin (2002), NRLMSISE-00 empirical model of the atmosphere: Statistical comparisons and scientific issues, *J. Geophys. Res.*, *107*(A12), 1468, doi:10.1029/2002JA009430.

Rastogi, R. G. (1977), Geomagnetic storms and electric fields in the equatorial ionosphere, *Nature*, *268*, 422–424, doi:10.1038/268422a0.

Rees, D., and T. J. Fuller-Rowell (1989), The response of the thermosphere and ionosphere to magnetospheric forcing, *Philos. Trans. R. Soc. London, Ser. A*, *328*, 139–171, doi:10.1098/rsta.1989.0029.

Richmond, A. D. (1973), Equatorial electrojet—I. Development of a model including winds and instabilities, *J. Atmos. Terr. Phys.*, *35*, 1083–1103, doi:10.1016/0021-9169(73)90007-X.

Richmond, A. D., and S. Matsushita (1975), Thermospheric response to a magnetic substorm, *J. Geophys. Res.*, *80*(19), 2839–2850, doi:10.1029/JA080i019p02839.

Ridley, A. J., A. D. Richmond, T. I. Gombosi, D. L. De Zeeuw, and C. R. Clauer (2003), Ionospheric control of the magnetospheric configuration: Thermospheric neutral winds, *J. Geophys. Res.*, *108*(A8) 1328, doi:10.1029/2002JA009464.

Rostoker, G., S.-I. Akasofu, J. Foster, R. A. Greenwald, Y. Kamide, K. Kawasaki, A. T. Y. Lui, R. L. McPherron, and C. T. Russell (1980), Magnetospheric substorms: Definition and signatures, *J. Geophys. Res.*, *85*(A4), 1663–1668, doi:10.1029/JA085iA04p01663.

Schunk, R. W., and A. F. Nagy (1978), Electron temperatures in the *F* region of the ionosphere: Theory and observations, *Rev. Geophys.*, *16*, 355–399, doi:10.1029/RG016i003p00355.

Schunk, R. W., and J. C. G. Walker (1973), Theoretical ion densities in the lower ionosphere, *Planet. Space Sci.*, *21*, 1875–1896, doi:10.1016/0032-0633(73)90118-9.

Senior, C., and M. Blanc (1984), On the control of magnetospheric convection by the spatial distribution of ionospheric conductivities, *J. Geophys. Res.*, *89*(A1), 261–284, doi:10.1029/JA089iA01p00261.

Siscoe, G. L., N. U. Crooker, G. M. Erickson, B. U. Sonnerup, K. D. Siebert, D. R. Weimer, W. W. White, and N. C. Maynard (2000), Global geometry of magnetospheric currents inferred from MHD simulations, in *Magnetospheric Current Systems*, *Geophys. Monogr. Ser*, vol. 118, edited by

S. Ohtani et al., pp. 41–52, AGU, Washington, D. C., doi:10.1029/GM118p0041.
Southwood, D. J. (1977), The role of hot plasma in magnetospheric convection, *J. Geophys. Res.*, *82*(35), 5512–5520, doi:10.1029/JA082i035p05512.
Spiro, R. W., R. A. Wolf, and B. G. Fejer (1988), Penetration of high latitude electric field effects to low latitudes during SUNDIAL 1984, *Ann. Geophys.*, *6*, 39–50.
Sugiura, M., and J. C. Cain (1966), A model equatorial electrojet, *J. Geophys. Res.*, *71*(7), 1869–1877, doi:10.1029/JZ071i007p01869.
Tanaka, T. (1995), Generation mechanisms for magnetosphere-ionosphere current systems deduced from a three-dimensional MHD simulation of the solar wind–magnetosphere-ionosphere coupling processes, *J. Geophys. Res.*, *100*(A7), 12,057–12,074, doi:10.1029/95JA00419.
Tarpley, J. D. (1970), The ionospheric wind dynamo—I. Lunar tide, *Planet. Space Sci.*, *18*, 1075–1090, doi:10.1016/0032-0633(70)90109-1.
Toffoletto, F., S. Sazykin, R. Spiro, and R. Wolf (2003), Inner magnetospheric modeling with the Rice Convection Model, *Space Sci. Rev.*, *107*, 175–196, doi:10.1023/A:1025532008047.
Tsunomura, S. (1999), Numerical analysis of global ionospheric current system including the effect of equatorial enhancement, *Ann. Geophys.*, *17*, 692–706, doi:10.1007/s00585-999-0692-2.
Tsunomura, S., and T. Araki (1984), Numerical analysis of equatorial enhancement of geomagnetic sudden commencement, *Planet. Space Sci.*, *32*, 599–604, doi:10.1016/0032-0633(84)90109-0.
Untiedt, J. (1967), A model of the equatorial electrojet involving meridional currents, *J. Geophys. Res.*, *72*(23), 5799–5810, doi:10.1029/JZ072i023p05799.
Vasyliunas, V. M. (1970), Mathematical models of magnetospheric convection and its coupling to the ionosphere, in *Particle and Field in the Magnetosphere*, edited by B. McCormac, pp. 60–71, D. Reidel, Hingham, Mass., doi:10.1007/978-94-010-3284-1_6.
Vasyliunas, V. M. (1972), The interrelationship of magnetospheric processes, in *Earth's Magnetospheric Processes*, edited by B. M. McCormac, pp. 29–38, D. Reidel, Norwell, Mass., doi:10.1007/978-94-010-2896-7_3.
Wei, Y., W. Wan, Z. Pu, M. Hong, Q. Zong, J. Guo, B. Zhao, and Z. Ren (2011), The transition to overshielding after sharp and gradual interplanetary magnetic field northward turning, *J. Geophys. Res.*, *116*, A01211, doi:10.1029/2010JA015985.
Wolf, R. A. (1970), Effects of ionospheric conductivity on convective flow of plasma in the magnetosphere, *J. Geophys. Res.*, *75*(25), 4677–4698, doi:10.1029/JA075i025p04677.
Wolf, R. A., R. W. Spiro, S. Sazykin, and F. R. Toffoletto (2007), How the Earth's inner magnetosphere works: An evolving picture, *J. Atmos. Sol. Terr. Phys.*, *69*(3), 288–302, doi:10.1016/j.jastp.2006.07.026.
Yoshikawa, A. (2002a), How does the ionospheric rotational Hall current absorb the increasing energy from the field-aligned current system?, *Geophys. Res. Lett.*, *29*(7), 1133, doi:10.1029/2001GL014125.
Yoshikawa, A. (2002b), Excitation of a Hall-current generator by field-aligned current closure, via an ionospheric, divergent Hall-current, during the transient phase of magnetosphere-ionosphere coupling, *J. Geophys. Res.*, *107*(A12), 1445, doi:10.1029/2001JA009170.
Yoshikawa, A. (2007), Cowling channel formation model in the 3D-ionosophere, paper presented at XXIV General Assembly, Int. Union of Geod. and Geophys., Perugia, Italy.
Yoshikawa, A., and M. Itonaga (1996), Reflection of shear Alfvén waves at the ionosphere and the divergent Hall current, *Geophys. Res. Lett.*, *23*(1), 101–104, doi:10.1029/95GL03580.
Yoshikawa, A., and M. Itonaga (2000), The nature of reflection and mode conversion of MHD waves at the inductive ionosphere: Multistep mode conversion between divergent and rotational electric fields, *J. Geophys. Res.*, *105*(A5), 10,565–10,584, doi:10.1029/1999JA000159.
Yoshikawa, A., O. Amm, H. Vanhamäki, and R. Fujii (2011a), A self-consistent synthesis description of magnetosphere-ionosphere coupling and scale-dependent auroral process using shear Alfvén wave, *J. Geophys. Res.*, *116*, A08218, doi:10.1029/2011JA016460.
Yoshikawa, A., A. Nakamizo, O. Amm, H. Vanhamäki, R. Fujii, Y.-M. Tanaka, T. Uozumi, K. Yumoto, and S. Ohtani (2011b), Self-consistent formulation for the evolution of ionospheric conductances at the ionospheric *E* region within the M-I coupling scheme, *J. Geophys. Res.*, *116*, A09223, doi:10.1029/2011JA016449.